Journal of Theoretical Biology xxx (xxxx) xxx

Contents lists available at ScienceDirect

Journal of Theoretical Biology

journal homepage: www.elsevier.com/locate/yjtbi

Deciphering the dynamics of lamellipodium in a fish keratocytes model

Laurent MacKay [a], Etienne Lehman [b], Anmar Khadra [a,*]

[a] Department of Physiology, McGill University, McIntyre Medical Building, 3655 Promenade Sir William Osler, QC H3G 1Y6, Canada
[b] Department of Mathematics, ENS Lyon, Lyon, France

ARTICLE INFO

Article history:
Received 18 July 2020
Revised 29 October 2020
Accepted 2 November 2020
Available online xxxx

Keywords:
Cell motility
Excitable media
Traveling waves
Kymograph analysis
Mathematical model
Slow-fast analysis
Bistability
Type IV excitability
Canards

ABSTRACT

Motile cells depend on an intricate network of feedback loops that are essential in driving cell movement. Integrin-based focal adhesions (FAs) along with actin are the two key factors that mediate such motile behaviour. Together, they generate excitable dynamics that are essential for forming protrusions at the leading edge of the cell and, in certain cases, traveling waves along the membrane. A partial differential equation (PDE) model of a self-organizing lamellipodium in crawling keratocytes has been previously developed to understand how the three spatiotemporal patterns of activity observed in such cells, namely, stalling, waving and smooth motility, are produced. The model consisted of three key variables: the density of barbed actin filaments, newly formed FAs called nascent adhesions (NAs) and VASP, an anti-capping protein that gets sequestered by NAs during maturation. Using parameter sweeping techniques, the distinct regimes of behaviour associated with the three activity patterns were identified. In this study, we convert the PDE model into an ordinary differential equation (ODE) model to examine its excitability properties and determine all the patterns of activity exhibited by this system. Our results reveal that there are two additional regimes not previously identified, including bistability and oscillatory-like type IV excitability (generated by three steady states and their manifolds, rather than limit cycles). These regimes are also present in the PDE model. Applying slow-fast analysis on the ODE model shows that it exhibits a canard explosion through a folded-saddle and that rough motility seen in keratocytes is likely due to noise-dependent motility governed by dynamics near the interface of bistability and type IV excitability. The two parameter bifurcation suggests that the increase in the proportion of rough motion is due to a shift in activity towards the bistable and type IV excitable regimes induced by a decrease in NA maturation rate. Our results thus provide important insight into how microscopic mechanical effects are integrated to produce the observed modes of motility.

1. Introduction

Cell migration plays a fundamental role in many physiological processes, including wound healing (Li et al., 2013), axonal growth (Zheng and ming Poo, 2007), immune response (Luster et al., 2005), as well as in pathophysiological processes such as cancer metastasis and thrombosis (Clark and Vignjevic, 2015; Ye et al., 2011). It is regulated by a complicated network of interacting proteins that generate complex dynamics essential for driving cellular motility (Pollard and Borisy, 2003; Huveneers and Danen, 2009; Zaidel-Bar et al., 2007; Seetharaman and Etienne-Manneville, 2019; Hanna and El-Sibai, 2013; Paszek et al., 2009; Stutchbury et al., 2017; Doyle et al., 2004). The formation of integrin-based protein complexes called focal adhesions (FAs) allows the front of the cell to adhere to a substrate when protruding forward, whereas their disassembly causes the cell to detach from the substrate while retracting in the back (Ballestrem et al., 2001). In other words, these FAs play a critical role as force-transmission sites which mediate cell movement. Such force is typically produced by the actin-cytoskeleton, with actin polymerization at the leading edge driving the protrusion of the membrane necessary for motility (Mogilner and Oster, 1996; Pollard and Borisy, 2003).

Cellular motility involves a number of complex spatiotemporal patterns of activity. For instance, in order for a cell to move in a directed fashion, it must first become rear-to-front polarized, a spatial pattern essential for cell movement. This is thought to occur as a result of mutual inhibitory feedback loops between two members of the Rho subfamily of GTPases; namely, Rac and Rho (Lin et al., 2012; Holmes et al., 2012). The mutual inhibitory interactions between these two proteins together with differences in diffusion coefficients in their active and inactive forms are used by the cell to produce spatially-segregated regions where the activity

* Corresponding author.
E-mail addresses: laurent.mackay@mail.mcgill.ca (L. MacKay), etienne.lehman@ens-lyon.fr (E. Lehman), anmar.khadra@mcgill.ca (A. Khadra).

https://doi.org/10.1016/j.jtbi.2020.110534
0022-5193/

of one GTPase is high and the other is low, while it is the opposite in the other region (Jilkine et al., 2007; Mori et al., 2008; Tang et al., 2018). These regions may be either protrusive (where Rac is elevated, promoting actin polymerization) or contractile (where Rho is elevated, promoting myosin-driven contraction of the actin cytoskeleton) (Edelstein-Keshet, 2016). Due the opposing effects of these two proteins on cell morphology, it is typical to denote the protrusive region as the front of the cell and the contractile region as the rear of the cell. In the absence of chemical cues, however, these protrusive and contractile regions may form randomly in a stochastic fashion, reducing the ability of the cell to exhibit directed movement (Lyda et al., 2019). Interestingly, within the context of motility, there are numerous other examples of coordinated patterns of activity, not only across space but also throughout time (MacKay and Khadra, 2020).

After a cell generates a rear-to-front polarization, its subsequent motility involves a number of key steps: (i) protrusion, (ii) adhesion, (iii) cell-body translocation, and (iv) de-adhesion (Ananthakrishnan and Ehrlicher, 2007). These steps can happen either continuously all at once or serially in a periodic manner. Often, whether a cell moves continuously or periodically is considered to be a phenotypic trait of a specific cell type (Lee et al., 1993; Lammermann and Sixt, 2009). For example, fish keratocytes are widely known to migrate continuously whereas Chinese hamster ovary (CHO-K1) cells exhibit cyclic protrusion/retraction cycles during their movement. This idea was investigated more thoroughly, first in Barnhart et al. (2011) and subsequently in Barnhart et al. (2017), by looking at a population of cells and quantitatively describing the observed qualitative variations in motility for one cell type. This is in contrast to the more common practice of focusing on a sub-population of cells whose motility is deemed to be representative of the cell type. Using such a comprehensive approach, it was found that within a population of fish keratocytes, some would move continuously while others exhibit waves of protrusion that travel from one end of the lamellipodium to another (Barnhart et al., 2017). In addition, individual cells could be switched between moving continuously or periodically by plating them on different substrates or treating them with pharmacological agents (Barnhart et al., 2017). This suggests that the same machinery is working to produce both modes of motility, but that the system can behave differently under varying conditions. A partial differential equation (PDE) model that account for barbed actin filament density, FA and VASP (an anti-capping protein that gets sequestered by newly formed FAs upon maturation) was developed and used to account for actin polymerization dynamics (Barnhart et al., 2017); this study ascertained that these differences in modes of motility could be explained by intercellular variations in the rates of various biochemical processes related to actin polymerization. By varying two key parameters in the model: VASP delivery rate and FA maturation rate, they identified the parameter regimes associated with the three modes of activity in fish keratocytes.

The formulation of the PDE model presented in Barnhart et al. (2017) assumed that actin polymerization is inhibited by capping proteins which prevent further growth of actin filaments, whereas the protein VASP exerts an anti-capping effect at the leading edge of the cell (Krause et al., 2002; Bear and Gertler, 2009). This anti-capping action allows for enough polymerization to occur in order for the collective force of polymerization of all filaments to overcome membrane tension and lead to protrusion in regions of sufficiently high actin filament density (Lacayo et al., 2007; Keren et al., 2008). Protrusion of the leading edge is highly correlated with the birth of new FAs called nascent adhesions (NAs) (Pontes et al., 2017), and their subsequent growth and stabilization into mature FAs (Choi et al., 2008). Interestingly, NA maturation have been shown to sequester VASP at the leading edge (Kuo et al., 2011), presumably antagonizing its anti-capping effect. If enough VASP is sequestered by FAs, the leading edge will stall, but if VASP is continually delivered to the leading edge (through an unspecified mechanism), it will eventually reach high enough levels to allow protrusion to restart. These positive and negative feedback processes produce the sequence of events which have been hypothesized to be the origin of the traveling waves of protrusion (Barnhart et al., 2017). Furthermore, based on results of the model and some experimental evidence in Barnhart et al. (2017), one may conclude that a typical fish keratocyte, exhibiting continuous motility, has a VASP delivery rate which outpaces the maturation of its adhesions, preventing its depletion at the leading edge by maturing NAs.

Although the PDE model presented in Barnhart et al. (2017) was quite alluring, providing important insights into the phenomenology observed in motile cells, it was not completely characterized. Indeed, the study focused primarily on experimental findings with the dynamic properties of the model left without being adequately investigated. One important feature of this model is that it was excitable. Excitable systems are known for their ability to generate very pronounced responses to small suprathreshold stimuli, with their state variables typically generating large excursions in state space (Keener et al., 2009; Gerhardt et al., 1990). If the models that describe these systems (i) produce an oscillatory response whose frequency can gradually become arbitrarily small as the magnitude of the stimulus is varied, then their excitability is referred to as type I; (ii) produce an oscillatory response for a given range of stimulus magnitude that abruptly turns off (i.e., becomes non-oscillatory) outside this range, then their excitability is referred to as type II; (iii) exhibit a single transient response regardless of the duration (and typically the magnitude) of the stimulus, then their excitability is referred to as type III (Hodgkin and Huxley, 1952). The presence of time-scale separation within such models allows them to produce these excitability properties as well as other very interesting dynamics including canards (Szmolyan and Wechselberger, 2001; Wechselberger et al., 2013), with significant implications on the behaviour of the physiological systems they meant to describe. Indeed, by including noise, the dynamics of these models become richer and more pronounced (Lindner et al., 2004). Example of such models that feature excitability properties are quite abundant, very commonly encountered when studying the electrophysiological properties of neurons and endocrine systems using ion-channel based models (Alexander et al., 2019; Mitry et al., 2020).

In this study, we use tools from non-linear dynamics and slow-fast analysis to investigate excitability properties of the model presented in Barnhart et al. (2017) and determine how it affects dynamics of cell motility in fish keratocytes. This is done by simplifying the PDE model into an ordinary differential equation (ODE) model and examining the underlying dynamics of this model in various parameter regimes in the absence and presence of noise. Our results show that this system possesses not only type I and III excitability, but also a new type of noise-induced excitability (referred to hereafter as type IV) only seen recently in a Hodgkin–Huxley type model of cerebellar stellate cells (Farjami et al., 2020). Using bifurcation theory and slow-fast analysis, we determine the bifurcation points that define the boundaries between the various regimes of behaviour obtained by the PDE model (including the newly discovered bistability and traveling wave pulse regimes), and uncover the underlying dynamics of the system particularly when exhibiting canard explosion.

2. The non-dimensionalized model

We begin by first considering the non-dimensionalized model of adhesion-dependent wave generation published in Barnhart et al. (2017). This model describes the movement of the leading edge of a cell driven by actin polymerization pushing against the

cell membrane and the biochemical feedback this process receives from interactions between the protein VASP and adhesion complexes anchoring the cell to its substrate. We present the 1-Dimensional spatiotemporal variant of the model, which simplifies a 2-Dimensional spatiotemporal lamellipodium model of the cell into an infinitesimally thin strip just behind the leading edge. As we will demonstrate later, this 1-Dimensional formulation captures the experimentally relevant behaviour of motile cells, while being simpler to analyze.

The spatiotemporal model presented in the supplemental material of Barnhart et al. (2017) is given by

$$\epsilon\frac{\partial}{\partial T}B(X,T) = (1+\eta_B V) - \frac{B}{1+AB/(1+M+KB)} + \epsilon^2\frac{\partial}{\partial X}\left(\frac{1}{\Gamma}\frac{\partial B}{\partial X}\right) + \Xi_t \quad (1)$$

$$\frac{\partial}{\partial T}A(X,T) = d - \frac{(1+\eta_A V+\eta_M MV)A}{1+M+KB}, \quad (2)$$

$$\frac{\partial}{\partial T}M(X,T) = RB - (\theta+\eta_M V)M, \quad (3)$$

where B is the actin barbed end density, M is the density of mature adhesions, A is the total local concentration of VASP, η_B is the increase in actin branching due to polymerization, R is the scaled maturation rate of nascent adhesions, θ is the scaled disassembly rate of mature adhesions, d is the scaled delivery rate of cytosolic VASP, η_A is the scaled VASP (rearward) advection rate, η_M is the scaled adhesion (rearward) advection rate, K is the ratio of affinities for the binding/unbinding of VASP-to-actin and VASP-to-adhesions, V is the local velocity of the leading edge given by

$$V = \begin{cases} 1-\left(\frac{B_c}{B}\right)^8 & B \geqslant B_c \\ 0 & \text{otherwise}, \end{cases} \quad (4)$$

with B_c being the critical barbed end density required to produce enough force to move the leading edge defined by

$$B_c = \begin{cases} \int B_c^0 & Vdx = 0 \\ \int (1+E)B_c^0 & Vdx > 0, \end{cases} \quad (5)$$

with $E = 0.1$ being the fractional increase in membrane tension when the leading edge is protruding, $0 < \epsilon < 1$ is a small parameter which quantifies how fast the dynamics of B are compared to A and M, $\Gamma = 1 + AB/(1+M+KB)$ is a non-dimensional auxiliary parameter related to the (lateral) advective transport of barbed ends due to actin polymerization, and Ξ_t is a Wiener process with autocorrelation $\langle \Xi(T)\Xi(T-T')\rangle = \Xi_0^2\delta(T-T')$. Numerical values for all parameters of the non-dimensional model are presented in Table 1. Furthermore, in order for the problem to be well-posed, we need two boundary conditions for the variable B. As in Barnhart et al. (2017), we choose Neumann boundary conditions, given by

$$\left.\frac{\partial B}{\partial X}\right|_0 = \left.\frac{\partial B}{\partial X}\right|_L = 0,$$

where L is the length of the domain. Consistent with the results in Barnhart et al. (2017), by using Dirichlet boundary conditions $B|_0 = B|_L = B_0 < B_c^0$, we obtain a similar model behaviour but with waves initiated closer to the middle of the domain than with Neumann boundary conditions (results not shown).

Table 1
Default parameter values of the model, adapted from Barnhart et al. (2017). No specific value is assigned to d as it is used as the main bifurcation parameter, and is taken from an appropriate range. Parameter ranges represent the physiologically expected lower and upper bounds of these parameters.

Parameter	Definition	Value	Range
d	VASP delivery rate	–	$]0,1]$
R	Adhesion maturation rate	0.2	$]0,4]$
η_B	Advection rate for B	1	–
η_A	Advection rate for A	1	–
η_M	Advection rate for M	1	–
K	VASP affinity ratio	1	$]0,2]$
θ	Degradation rate of mature adhesions	0.05	$]0,1]$
B_c^0	Basal critical barbed actin density	4	-
E	Fractional increase in membrane tension	0.1	$]0,1]$
ϵ	Timescale difference of the fast variable	0.1	$]0,1]$

3. The simplified model

In order to simplify our analysis of the model, we move from a PDE setting where dynamics vary across space and time to an ODE setting where we are essentially considering the intrinsic dynamics of one point along the leading edge. We will demonstrate later that the ODE model captures the underlying dynamics of the PDE model very accurately.

Model conversion to an ODE setting is achieved by simply removing the diffusion-like $\partial_X\left(\Gamma^{-1}\partial_X B\right)$ term in Eq. (1), which eliminates the dependence of the function B, A, and M on the spatial variable X, as well as setting $E = 0$. We will discuss these assumptions in more detail in Section 5. These simplifications yield the system,

$$\epsilon\frac{d}{dT}B(T) = (1+\eta_B V) - \frac{B}{1+AB/(1+M+KB)} + \Xi_t \quad (6)$$

$$\frac{d}{dT}A(T) = d - \frac{(1+\eta_A V+\eta_M MV)A}{1+M+KB} \quad (7)$$

$$\frac{d}{dT}M(T) = RB - (\theta+\eta_M V)M, \quad (8)$$

where all variables and parameters are the same as before. For compatibility with the numerical continuation software AUTO-07p (Doedel et al., 2007) that we have used to analyze the dynamics of the model, we have slightly modified Eq. (4) to make it a continuously differentiable function, given by

$$V = \begin{cases} \exp\left[\frac{-\lambda}{B-B_c}\right]\left(1-\left(\frac{B_c}{B}\right)^8\right) & B \geqslant B_c \\ 0 & \text{otherwise} \end{cases}, \quad (9)$$

where $0 < \lambda \ll 1$ is a small parameter. Notice that by making $\lambda \to 0$, this velocity function defined by Eq. (9) becomes an arbitrarily good approximation for the velocity function defined by Eq. (4) (see Fig. 1A). We have also quantified the error that this approximation introduces into the model by finding $\overline{B}$, the value of B where $\partial V/\partial B$ reaches its maximum. The original velocity function defined by Eq. (4) has its maximal slope at $B = B_c$, whereas Eq. (9) has its maximal slope at $\overline{B} > B_c$. Therefore, by evaluating the difference $\overline{B} - B_c$, we obtain a simple way of quantifying the error in our approximation. As can be seen in Fig. 1B, this error metric increases monotonically with λ and in the limit as $\lambda \to 0$, we have $\overline{B} \to B_c$. Throughout this chapter, we have used values of λ that are as small as possible while ensuring numerical stability, choosing it to be within the range $\lambda \in \left[10^{-5}, 10^{-2}\right]$ (see grey region in Fig. 1B).

In this section, we will not consider the effects of noise on the system and thus set $\Xi_t = 0$. Under these assumptions, the model becomes a simple deterministic system of ODEs which we will now analyze to understand how the intrinsic dynamics of a single point are reflected in the traveling wave solutions in the PDE model.

3.1. The stalled equilibrium

From the form of Eq. (4), it is clear that the dynamics of the ODE system may be divided into two regimes that are separated by the

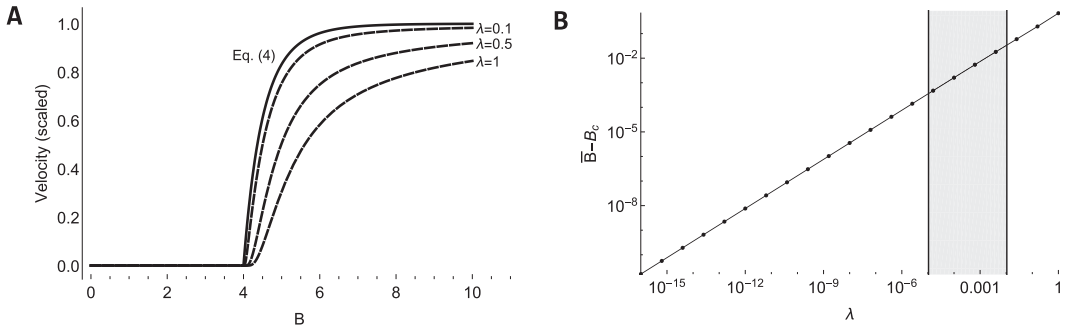

Fig. 1. (A) Velocity function as defined by Eq. (4) (solid line) and as defined by Eq. (9) (dashed lines) for different values of λ. (B) Convergence measure showing the difference between the maximum slope B of the velocity function defined by Eq. (9), denoted by $\bar{B}$, and that defined by Eq. (4), denoted by B_c. The smaller the λ, the smaller this convergence measure.

plane $B = B_c$. In the regime with $B < B_c$, we have $V = 0$ and the cell is stalled due to insufficient actin polymerization; this produces a simpler dynamical system for which we may solve for its steady state, the stalled equilibrium (B_0, A_0, M_0), given by

$$B_0 = \frac{1}{1-d},\ A_0 = \frac{d(\theta(-d+K+1)+R)}{\theta(1-d)},\ M_0 = \frac{R}{(1-d)\theta}. \tag{10}$$

From these expressions, it is clear that stalled equilibrium is only biophysically-relevant for $d < 1$, as for $d > 1$ the stalled equilibrium will not be in the positive octant of state space. We may further investigate the stability of this equilibrium by evaluating the Routh-Hurwitz criterion. This criterion requires that the coefficients of the characteristic polynomial of the system given by $P(s) = s^3 + a_1 s^2 + a_2 s + a_3$ satisfy $a_1, a_3 > 0$ and $a_1 a_2 > a_3$. The characteristic polynomial for this system, evaluated at the stalled equilibrium, is given by

$$\begin{aligned} P(s) = \ & s^3 \\ & + s^2 \frac{\theta\left(\theta(-d+K+1)-(d-1)\left(\epsilon\left((d-1)^2+K\right)+1\right)\right)+R\left((d-1)^2\epsilon+\theta\right)}{\theta(-d+K+1)+R} \\ & - s\frac{(d-1)\theta\left(\epsilon\left(d^2+\theta\left((d-1)^2+K\right)-2d+R+1\right)+\theta\right)}{\theta(-d+K+1)+R} \\ & - \frac{(d-1)^3\theta^2\epsilon}{\theta(-d+K+1)+R}. \end{aligned}$$

From these criteria, we may conclude that the non-negative model parameters along with the constraint $d < 1$ are necessary and sufficient conditions for the stalled equilibrium to be stable (see Appendix A for details).

From the force–velocity relationship (given by Eq. (4)), we can see that $V = 0$ is only valid for $B \leqslant B_c$. Based on the expression for B_0, we can conclude that $B_0 = B_c$ when $d = d_0 := (B_c - 1)/B_c$. Therefore, the stalled equilibrium is a physiologically-relevant stable steady state whenever $d < (B_c - 1)/B_c$. This means that, for $B > B_c$, the stalled equilibrium is no longer a fixed point of the system and only physiologically-relevant whenever $d < d_0 = (B_c - 1)/B_c$. We will demonstrate in the next section that in the limit as $\lambda \to 0$, there is a Hopf bifurcation at $d = d_0$ and the stalled equilibrium gets replaced completely by an unstable steady state in a continuous manner (because V in Eq. (9) is continuous).

3.2. Modes of motility

When $B > B_c$ (i.e., $d > d_0$), we have $V = 1 - (B_c/B)^8$, producing various modes of motility in the model. In this regime, the nonlinearity of V makes obtaining analytical results challenging. To resolve this issue, we use here numerical continuation methods in AUTO to produce bifurcation diagrams that explain how the behaviour of the system changes as certain parameter values are varied.

For the parameter values listed in Table 1, we observe that for a small enough d, the eigenvalues of the Jacobian matrix for Eqs. (6)–(8) evaluated at the stalled equilibrium (i.e., at $V = 0$) have a complex conjugate pair with negative real part. Indeed, by plotting the bifurcation diagram of scaled actin barbed end density B, whose dynamics are determined by the complete ODE system (6)–(8) coupled to Eq. (9), with respect to scaled VASP delivery rate d, we obtain a branch of stable steady states (see black solid lines in Fig. 2) that undergoes a subcritical Hopf bifurcation HB1 at $d_{\mathrm{HB1}} = (1 + \varepsilon(\lambda))d_0$, where $0 < \epsilon(\lambda) \ll 1$ is an increasing function of λ.

In the limit as $\lambda \to 0$, HB1 shifts to $d = d_0$, a scenario that corresponds to the original definition of V given by Eq. (4). As stated before, the remaining analysis is performed for very small λ such that Eq. (9) is as close to Eq. (4) as possible. Based on this, two unstable branches of limit cycles (i.e., envelopes of periodic orbits representing the maximum and minimum of these orbits) emerge from HB1 at $d \approx d_0$. These unstable branches undergo saddle-node bifurcation of periodic orbits at $d_{\mathrm{SNP}} < d_{\mathrm{HB1}}$ (see inset in Fig. 2A) followed by a canard explosion, forming two stable branches of limit cycles (solid blue lines) with large-amplitude oscillatory solutions that eventually plateau at higher d values (see Fig. 2A). These periodic branches eventually terminate at a homoclinic bifurcation HM1 at d_{HM1} (the terminal points of these branches), a key feature of type I excitability.

Beyond $d \approx d_0$, the branch of unstable steady states then forms two folds of saddle-node bifurcations SN1 and SN2 at $d = d_{\mathrm{SN1}} \geqslant d_0$ and $d = d_{\mathrm{SN2}}$, respectively. This branch of unstable steady states eventually becomes stable (solid black line) when crossing a Hopf bifurcation HB2 at $d = d_{\mathrm{HB2}} \geqslant d_{\mathrm{SN2}}$, where two small branches (or envelopes) of unstable periodic orbits (dashed blue lines) emerge and terminate at a homoclinic bifurcation HM2 at $d = d_{\mathrm{HM2}}$. This latter homoclinic HM2 coincides with the previous homoclinic HM1 at $d_{\mathrm{HM2}} = d_{\mathrm{HM1}}$. The resulting new stable branch of steady states for $d > d_{\mathrm{HB2}}$ represents the smooth motile equilibria with a constant speed $V > 0$.

Based on this bifurcation structure of Fig. 2A, we may conclude that system (6)–(8) exhibits one very small regime of bistability between the stalled equilibrium and oscillatory solution when $d_{SNP} < d < d_{\mathrm{HB1}}$ (see inset). This regime is so small, it is very difficult to discern HB1 from SNP. It also exhibits coexistence between the stable smooth motile equilibrium and two unstable steady states between $d_{\mathrm{HM2}} < d < d_{\mathrm{SN1}}$, allowing trajectories of system (6)–(8) to exhibit noise-induced repetitive and large transient excursions around the motile steady state. These transient excursions/oscillations (to be discussed in more detail in Section 4.1) have trajectories reminiscent of the previously described oscillatory solutions and exhibit many properties of type III excitability. However, the geometric objects governing their dynamics are

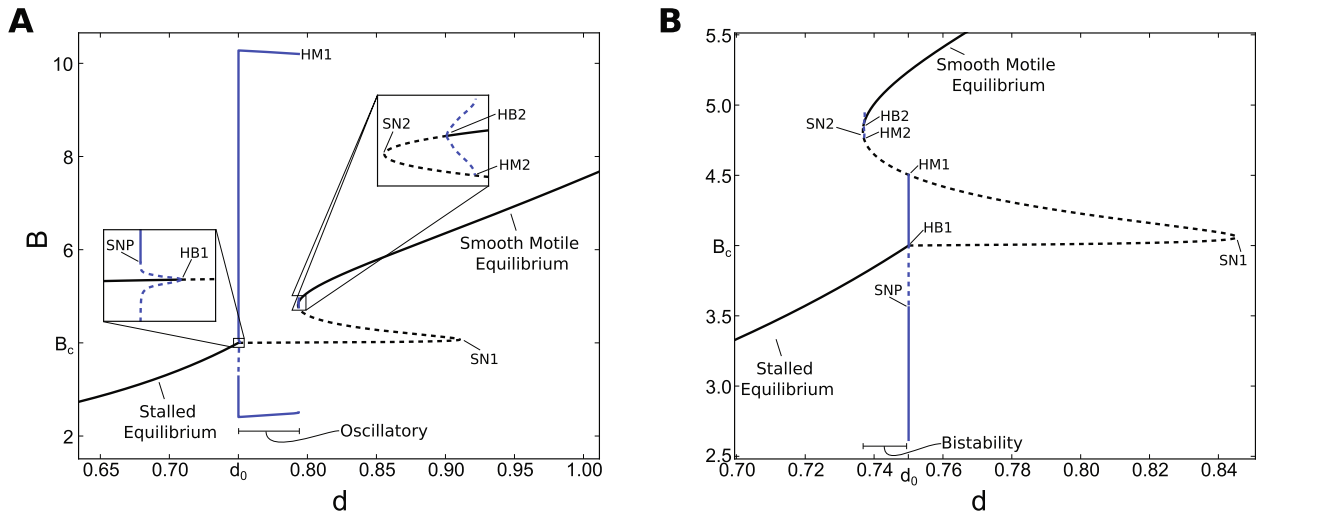

Fig. 2. One-parameter bifurcation analysis of the full system defined by Eqs. (6)–(8). The bifurcation diagram of actin barbed end density B with respect to the scaled VASP delivery rate d at two different values of the scaled nascent adhesion maturation rate: (A) $R = 0.1$, and (B) $R = 0.065$. Black solid (dashed) lines indicate stable (unstable/saddle) branches of equilibria; blue solid (dashed) lines correspond to branches or envelopes of stable (unstable) limit cycles. There are five branches of stable and unstable/saddle equilibria in panel A; they are separated by a subcritical Hopf bifurcation HB1 (at $d \approx d_0$), two saddle-node bifurcations SN1 and SN2 and a second subcritical Hopf bifurcation HB2. The branch of stable steady states prior to/beyond HB1/SN2 corresponds to the stalled/smooth motile equilibria, respectively. Two branches of unstable periodic orbits emerge from HB1 but quickly turn into stable branches at a saddle-node bifurcation of periodic orbits SNP (see inset). These stable periodic branches then expand vertically, forming a canard explosion until they eventually plateau and terminate at a homoclinic bifurcation HM1, defining an oscillatory regime ($d_{SNP} \leqslant d < d_{HM1}$). Similarly, two branches of unstable periodic orbits emanate from HB2 and terminate at a homoclinic bifurcation HM2. The oscillatory regime shrinks significantly in panel B with the canard explosion colliding with the saddle branch between SN1 and SN2, and bistability is formed between the stalled and smooth motile equilibria. Insets around the Hopf bifurcations have not been included in panel B, as they would be qualitatively identical to those in panel A.

distinct from those at play during type III excitability, and thus we refer to this dynamical behaviour as type IV excitability (Mitry et al., 2020; Farjami et al., 2020).

By decreasing the value of the scaled maturation rate of nascent adhesions R, one can make d_{SN2} smaller than d_0 and cause the branches of stable periodic orbits to terminate at the homoclinic bifurcation HM1 located on the branch of unstable steady states connecting the two saddle-nodes SN1 and SN2 (see Fig. 2B). Notice that, according to this configuration, periodic oscillations only exist for a small parameter regime at $d \approx d_{HB1}$, and that the system exhibits bistability between the stalled and motile equilibria for $d_{HM2} < d < d_{SNP}$. It thus follows that, depending on how d_{SN2} compares to d_0, the system may either exhibit an oscillatory regime as in Fig. 2A or a regime of bistability as in Fig. 2B.

Thus, in summary, system (6)–(8) can exhibit four possible dynamic behaviours that may coexist. This includes the stalled equilibrium (type III excitable) for $d < d_0$, a smooth motile equilibrium that is not excitable (type IV excitable) for $d > d_{SN1}$ ($d_{HM1} < d < d_{SN1}$), and either an oscillatory solution (type I excitable) with $d_{SNP} < d < d_{HM1}$ or coexistence between the stalled and smooth motile equilibria for $d_{HM2} < d < d_{SNP}$. To further understand how these different monostable and bistable regimes govern dynamics of the PDE model, defined by Eqs. (1)–(3), one needs to plot the two-parameter bifurcation of the system defined by Eqs. (6)–(8) with respect to both the scaled VASP delivery rate d and the scaled maturation rate of nascent adhesions R. Doing so will provide insights into how these regimes manifest themselves in the d, R-parameter space. This is done in detail in the following section.

3.3. Two-parameter bifurcation

In order to compare the various regimes of behaviour associated with the PDE model defined by Eqs. (1)–(3) and introduced in Barnhart et al. (2017), we have continued all the bifurcation points discussed in Fig. 2 within the (d, R)-plane of parameter space (see

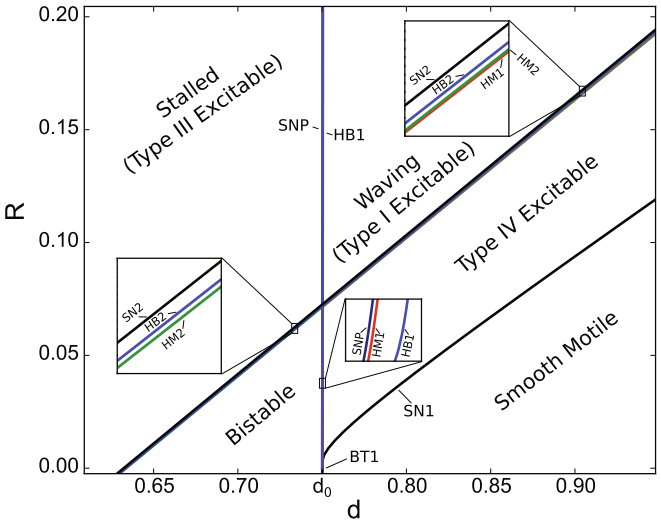

Fig. 3. The various regions of behaviour associated with the full system, given by Eqs. (6)–(8), plotted as two-parameter bifurcation with respect to the scaled nascent adhesion maturation rate R and scaled VASP delivery rate d. The boundaries of these regions are determined by tracking the bifurcation points identified in Fig. 2. We observe five distinct regions in parameter space: stalled regime, the bistable regime, the oscillatory regime, the type IV excitable regime, and the smooth motile regime. The excitability properties of some of these regimes are specified between parentheses. The bistable and type IV excitable regimes are novel findings, whereas the other regimes had been reported in Barnhart et al. (2017).

Fig. 3). The resulting two-parameter bifurcation diagram delineates the different monostable and bistable regimes identified in the previous section. Indeed, as shown in Fig. 3, the regimes identified in the two-parameter bifurcation follow very closely the map describing the behaviour of the PDE model. Notably, we obtain 5 distinct and discernible regimes: (i) a monostable stalled regime possessing only the stalled equilibrium, bounded to the right by the saddle-node bifurcation of periodic orbits SNP (which happens

to be indiscernibly close to the Hopf bifurcation HB1) and from below by the saddle-node bifurcation SN2; (ii) a monostable oscillatory regime possessing stable oscillatory solutions, bounded to the left by HB1 and to the right by the homoclinic bifurcation HM1 (in red, see inset) coinciding with the homoclinic bifurcation HM2 (in green, see inset); (iii) a bistable regime between the stalled and smooth motile equilibria, bounded to the left/top by HM2 or SN2 and to the right by SNP; (iv) a smooth motile regime possessing the smooth motile equilibrium, bounded from the top by the saddle-node SN1; (v) a type IV excitable regime possessing the smooth motile equilibrium, bounded to the left by the HB1, from the top by HM1 and from the bottom by SN1. Within this configuration, additional very small regimes also exist. Namely, a bistable regime between the stalled equilibrium and oscillatory solution between SNP and HB1, as well as a bistable regime between the smooth motile equilibrium and the oscillatory solution between HB2 and HM1.

The fact that some of these regimes match well with those previously identified with the PDE model (see Fig. 6A in Barnhart et al., 2017) and further identifies new ones not previously discovered in Barnhart et al. (2017) suggests that the spatiotemporal patterns produced by the PDE model can be understood from the intrinsic dynamics of the ODE model. Interestingly, we have identified a novel regime, the type IV excitable regime. This regime is separated from the previously identified smooth motile regime by the continuation of SN1, which is depicted in Fig. 3 as a line that terminates at the Bogdanov-Takens bifurcation BT1 where it collides with HB1 and SNP at $(d_0, 0)$. As we shall see in Section 4.3, when the system is between HM1 and SN1, it is sensitive to the presence of noise, leading to stochastically-induced transient oscillations despite the fact that the system only possesses one stable fixed point.

4. Slow-fast analysis

As indicated by Eqs. (6)–(8), setting $\epsilon \ll 1$ generates a time scale separation, making the variable much faster than A and M. Thus to understand dynamics, one can apply slow-fast analysis on the full system by dividing it into one fast variable and two slow variables. Within the context of this analysis, we can obtain the critical manifold S of system (6)–(8), determined by the steady states of the fast subsystem B as a function of the slow subsystem defined by A and M, and decomposing it into attracting and repelling sheets that are typically separated by folds in S. An attracting (repelling) sheet of a critical manifold is defined as the set all points $\mathbf{p} \in \mathscr{S} \subset S$ that make all the eigenvalues of $(D_{\mathbf{x}}\mathbf{f})(\mathbf{p})$ have negative (positive) real parts, where $\mathbf{x}$ is the fast subsystem (i.e., $x = B$ in the model under consideration) and $\mathbf{f}$ is the right hand side of the ODE defining the fast subsystem (i.e., $\mathbf{f} = dB/dT$ in the same model). If a sheet is neither attracting nor repelling, it is said to be of saddle type. However, since our fast-subsystem is of dimension one, the critical manifold cannot have any sheets of this type. For a system with one fast and two slow variables (e.g., system (6)–(8)), the fold points separating attracting and repelling sheets form smooth curves (Desroches et al., 2012) that are typically curves of saddle-nodes for the fast subsystem.

In other words, for system (6)–(8), we define the critical manifold to be the null-surface of the fast variable B, given by

$$S = \{(B, A, M) : dB/dT = 0\}.$$

Similar to our analysis of equilibria, it is useful to decompose the critical manifold into two parts $S = S_V \cup S_0$ that correspond to when $V > 0$ and $V = 0$; $F^{\pm}$ are the folds of the critical manifold S, whereas S_V and S_0 are the sheets defined by

$$S_V = \{(B \geqslant B_c, A, M) : dB/dT = 0\}$$

and

$$S_0 = \{(B < B_c, A, M) : dB/dT = 0\}.$$

In the limit of $\lambda \to 0$, we may further subdivide the critical manifold into three distinct sheets, according to their stability properties. Two of these sheets are attracting while the other is repelling; the very top, labeled S_V^a, and very bottom S_0 are attracting, whereas the middle one, labeled S_V^r, is repelling. The sheets S_0 and S_V^a are separated from S_V^r by folds of saddle-nodes of the fast subsystem. Notice that $S_V = S_V^r \bigcup S_V^a$. When we have $\lambda > 0$, there is a fourth attracting sheet which extends from the upper edge of S_0 to the lower edge of S_V^r, where it meets the latter at a fold (in the limit $\lambda \to 0$ this attracting sheet shrinks down to nothing and the fold becomes arbitrarily sharp).

Superimposing the cubic-like curve formed by the intersection of the two A- and M-nullsurfaces (red curve in Fig. 4) onto the critical manifold can generate up to three intersections with S; these intersections can lie on any sheet of S. We will refer to this red line as the nullcurve hereafter. Using this configuration and the steady states formed by these intersections, one can decipher the dynamics of the full system in various parameter regimes (see Fig. 4).

Due to the presence of time-scale separation, the system exhibits slow and fast epochs; during the slow epochs, trajectories travel along the critical manifold, whereas during the fast epochs, dynamics of the fast variable dominate causing trajectories to jump between sheets of the critical manifold. These jumps occur towards the end of each slow epoch when solution trajectories approach a fold (or a saddle-node) in the critical manifold. In other words, the critical manifold locally organizes the dynamics of the full system according to its slow and fast subsystems.

Although the condition $\epsilon \ll 1$ is required to observe the slow-fast dynamics, the choice of ϵ is somewhat arbitrary. Specifically, we observe that for $\epsilon = 0.1$, much of the system's dynamics can be well understood using the critical manifold and its two folds, suggesting that, in the oscillatory regime, the system acts as a relaxation oscillator (see Fig. 4C) (van der Pol, 1926). Nonetheless, in the analysis presented here, we will study the underlying dynamics of this system in various parameter regimes to understand how it behaves and how noise can produce interesting outcomes.

4.1. The stalled and bistable regimes

As discussed above, the system has a stalled equilibrium when $d < d_0$ (in the limit as $\lambda \to 0$). In Barnhart et al. (2017), it was stated that this regime is excitable, but a precise characterization of that excitability was not provided. To do so, we begin first by focusing on the scenario where the stalled equilibrium is the sole attractor for the system (i.e., when $d_{\mathrm{HB2}} > d_0$). With this scenario, we obtain only one point of intersection representing the stalled equilibrium, formed by S_0, the bottom attracting sheet of the critical manifold S, and the nullcurve (see filled circle in Fig. 4A). By applying "small" perturbations away from the stalled equilibrium, we obtain graded responses that relaxes back to S_0 where the system will relax more slowly to the stalled equilibrium (see the short green line landing on the filled circle in Fig. 4A). Such behaviour is very intuitive, as small amplitude noise leads to small fluctuations around the stalled equilibrium (see time series simulations in Fig. 4A). However, when perturbations push the system beyond the repelling sheet S_V^r, solution trajectories shoot up to the attracting sheet S_V^a and then travel along this sheet until they cross the fold delimiting S_V^r and then jump down to S_0 where they relax back to the stalled equilibrium. Such behaviour is one of the hallmarks of type III excitability, where a suprathreshold perturbation must be applied for the full system to exhibit a large transient excursion (see

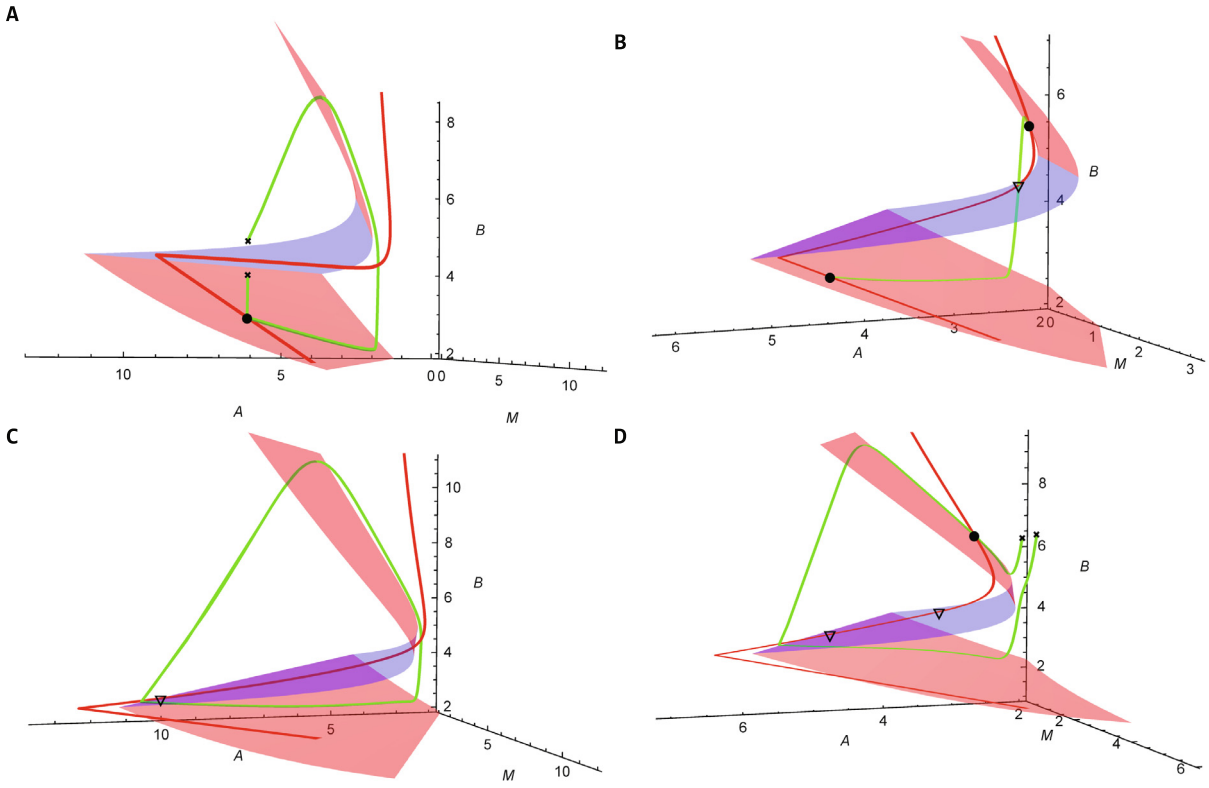

Fig. 4. Slow-fast analysis of the full system defined by Eqs. (6)–(8). The critical manifold S is depicted as a red surface, and the cubic-like nullcurve of the slow subsystem, defined as the intersection of the A- and M-nullsurfaces, is plotted as a red line. S consists of three sheets, two of which (the very top and bottom) are attracting (red surfaces) while the other is repelling (blue surface). The intersection of S with the nullcurve are the fixed points of the system, where stable fixed points are depicted as filled circles, and unstable (saddle) fixed points are depicted as open triangles. The number of fixed points and their stability define different regimes of model behaviour: (A) stalled ($d = 0.65, R = 0.15$), (B) bistable ($d = 0.72, R = 0.04$), (C) oscillatory ($d = 0.8, R = 0.15$), and (D) type IV excitable ($d = 0.8, R = 0.05$). Superimposing solution trajectories (green lines) illustrate the transient and steady state dynamics of the full system. In general, during slow epochs, trajectories travel along the attracting sheets of the critical manifold while during fast epochs they jump from one sheet to another. When relevant, initial conditions for trajectories are depicted as a black x symbol. (For interpretation of the references to colour in this figure legend, the reader is referred to the web version of this article.)

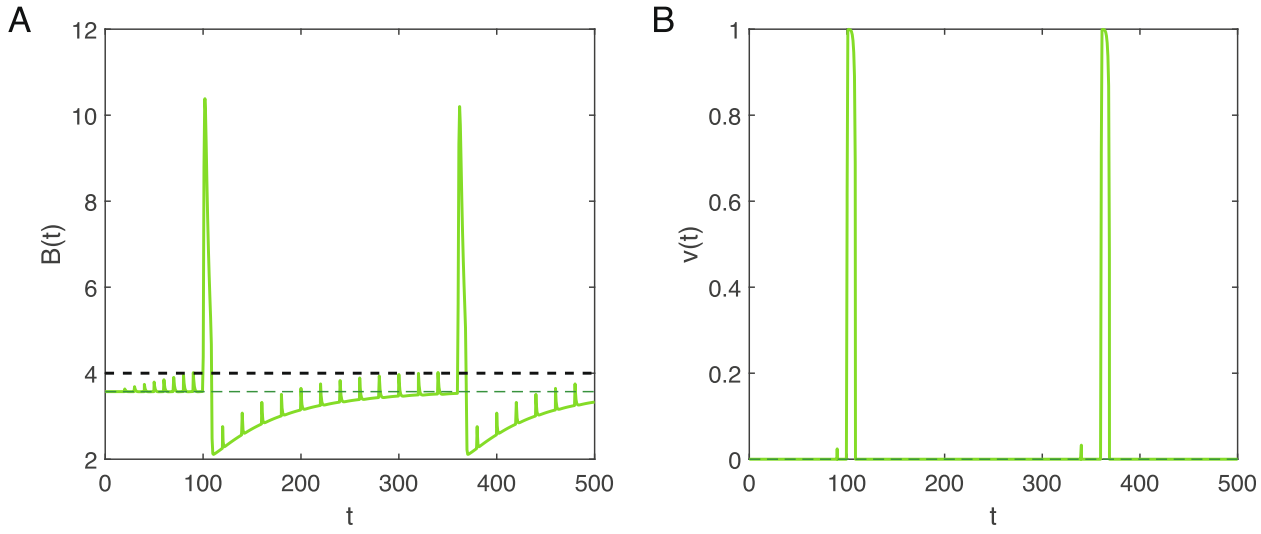

Fig. 5. Excitable dynamics obtained in the stalled regime possessing type III excitability. Impulsive perturbations are given to the system every 10 s when $t \in [20, 90]$ with increasing magnitudes and every 20 s when $t \in [100, 400]$ with a constant magnitude. (A) Time series simulations of actin barbed end density $B(t)$ in the absence of perturbations (dashed green line), showing that it remains at its fixed point near $B = 3.5714$ (i.e., the stalled equilibrium), and in the presence of perturbations (solid green line) that become suprathreshold, surpassing $B_c = 4$ (dashed black line). Notice that, in the latter case, we have "all or none" response in which subthreshold perturbations evoke only graded responses, whereas suprathreshold perturbations evoke large excursions, and that the return to the stalled equilibrium the system exhibits a "refractory period" where perturbations do not induce large excursions until the system is sufficiently close to the stalled equilibrium. (B) Time series simulations of the velocity $V(t)$. When $B > B_c$ the velocity becomes non-zero and drops back to zero when $B < B_c$. Here we have used $\delta = 0.72$. (For interpretation of the references to colour in this figure legend, the reader is referred to the web version of this article.)

Fig. 5A). Due to the fact that $B(t)$ crosses B_c at every excursion, the local velocity of the leading edge V quickly jumps between its two extreme values as in Fig. 5B.

In the bistable regime (i.e., when $d_{\mathrm{HB2}} < d < d_0$), on the other hand, we obtain, as expected, two points of intersections between the stable sheets of S and the nullcurve (see Fig. 4B). These intersections represent the stable stalled and motile equilibria. The behaviour of the full system in this regime is similar to that observed in the stalled regime when it comes to exhibiting graded responses to "small" perturbations away from either one of the two steady states by relaxing quickly to the closest attracting sheet and then moving slowly along this sheet towards the same steady state. However, if perturbations push the system beyond a threshold (see Section 4.3 for more about this threshold), trajectories travel to the other steady state (see Fig. 4B). Unlike the stalled regime, in this bistable regime, the steady state the system converges to depends on the perturbation applied and/or the initial condition of the system.

4.2. Relaxation oscillations

When the periodic branches of Fig. 2A (blue lines) exhibit a plateau phase for $d \in [d_{HB1}, d_{HM1}]$, the system behaves like a relaxation oscillator in a manner similar to the van der Pol oscillator (van der Pol and van der Mark, 1928). Slow-fast analysis reveals that the underlying dynamics of the system in this regime does indeed behave that way (see Fig. 4C). The critical manifold and the nullcurve, in this case, intersect only once in the middle repelling sheet S_V^r (blue surface in Fig. 4C), producing a saddle fixed point (open triangle) surrounded by a periodic orbit (green line) that jumps between the two attracting sheets S_0 and S_V^a (red surfaces in Fig. 4C). This periodic orbit exhibits relaxation-type oscillations by staying close to the upper and lower attracting sheets during the slow phase and jumping between them during the fast phase.

4.3. Type IV excitability

4.3.1. Deterministic dynamics

As indicated in Fig. 2A, when $d_{HM2} < d < d_{SN1}$, the only stable attractor is the smooth motile equilibrium and thus one would expect the system to exhibit motility with a constant velocity $V > 0$. However, as we discussed in the previous section, in such a scenario, it is possible to obtain transient oscillatory-like behaviour in the presence of noise. Indeed, in this regime, the system has three equilibria, one of which is stable and represents the smooth motile equilibrium, while the other two are of saddle type. For $d \approx d_{\mathrm{HM2}} (= d_{\mathrm{HM1}})$, the smooth motile equilibrium is very close to the middle saddle fixed point, which means that small perturbations may push the system past the stable manifold of this saddle (see Fig. 2). In the deterministic case, the stable manifold of the saddle acts as a separatrix which divides phase space into distinct regions, each of which contains the family of trajectories that converge to the system's distinct attractors (e.g., the smooth motile equilibrium). Although the smooth motile equilibrium is the only attractor in this regime, sufficiently large perturbations can push the system across the stable manifold of the saddle, causing trajectories to undergo large excursions away from the stable equilibrium before it returns back to this attractor (see the two trajectories (green lines) in Fig. 4D that start from close but distinct initial conditions). We have previously called this noise-dependent oscillatory-like behaviour of the system type IV excitability and the parameter regime associated with it the type IV excitable regime.

In Section 4.1, we have seen how the repelling middle sheet S_V^r of critical manifold acts as a threshold for excitation of the system, producing large excursions once perturbations push the system beyond the threshold. Such statements only make sense in the context of slow-fast analysis, and it is understood that the critical manifold is only an approximation of the true "slow manifold" which governs the dynamics for $\epsilon > 0$ (Hasan et al., 2018). This type of excitability is frequently discussed in the context of the Fitzhugh-Nagumo and Morris-Lecar models and labeled type III excitability. It should be distinguished from the one observed here in the type IV excitability regime, whereby dynamics are not governed by the critical manifold, but rather by the stable manifold of the saddle fixed point in a configuration that includes two additional steady states, the stable smooth motile equilibrium and another upper saddle fixed point. This type of excitability with single transient spikes is reminiscent to that observed in a Hodgkin–Huxley type model previously characterized by our group (Mitry et al., 2020; Farjami et al., 2020).

To better illustrate how the stable manifold of this saddle fixed point along with other manifolds organize trajectories, we have computed in Fig. 6 the stable and unstable manifolds of the two saddle fixed points (open triangles) lying to the left of the stable node (filled circle), i.e., the smooth motile equilibrium. In Fig. 6, we can see that the right saddle fixed point has a two-dimensional stable manifold (red surface) and a one-dimensional unstable manifold (blue line), whereas the left saddle fixed point has a one-dimensional stable manifold (red line) and a two-dimensional unstable manifold (blue surface). The red surface accumulates to the left with the red line, generating a hollow space further to the left, thereby allowing the passage of solution trajectories. Indeed, from the viewing angle used in Fig. 6, we may observe that solutions starting from two different initial conditions lying on either side of the red stable manifold exhibit significantly different propagation patterns (green curves). A trajectory starting from the left converges quickly to the stable node, while the other starting from the right generates a large loop around the manifold that takes advantage of the hollow space to return back to the stable node. In other words, the stable manifold of the right saddle

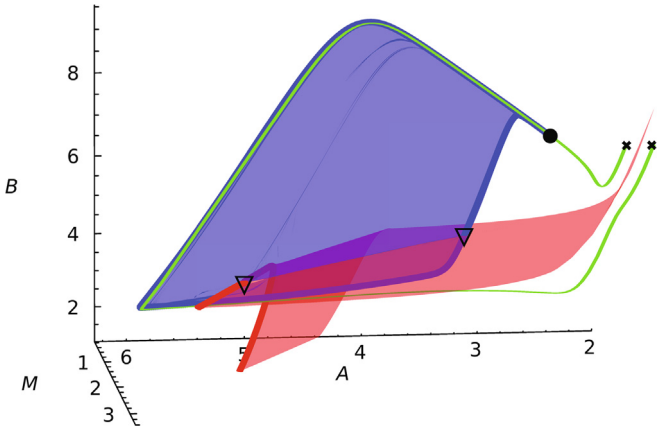

Fig. 6. The topology of the stable and unstable manifolds associated with the saddle fixed points govern the dynamics of excitability in the type IV excitable regime. Three steady states are present in this regime, a stable node representing the smooth motile equilibrium to the right (filled circle), and two saddle fixed points to the left (open triangles). The right saddle fixed point has two-dimensional stable manifold (red surface) and one-dimensional unstable manifold (blue line), while the left saddle fixed point has one-dimensional stable manifold (red line) and two-dimensional unstable manifold (blue surface). Two solution trajectories starting from different initial conditions (depicted by a black x symbol) are also plotted as green lines, one of which is initiated to the left of the red surface and one to the right of the red surface. The former quickly converges to the stable node, generating a graded response, while the latter elicits an excursion around the red surface that escapes from the hollow space to the right of the blue line back to the stable node, generating a pronounced response. (For interpretation of the references to colour in this figure legend, the reader is referred to the web version of this article.)

fixed point determines if the system undergoes a large excursion following a perturbation and acts as a " threshold" between pronounced and graded responses. This highlights the difference between this type of excitability and the one seen in type III oscillators.

4.3.2. Noise-dependent dynamics

We now consider what happens in the type IV excitability regime in the presence of noise (i.e., when $\left\langle \Xi_t^2 \right\rangle > 0$), where Ξ_t accounts for stochasticity arising from discrete effects in biochemical reactions (Gillespie, 2002). These discrete effects motivate the discussion of perturbations on solution trajectories. Intuitively, we may expect these perturbations to cause $B(T)$ to fluctuate around its equilibrium position B^*. We find that once the system becomes ergodic, the distribution $B(T)$ is well approximated by a normal distribution $B \sim \mathcal{N}(B^*, 12\Xi_0)$, where the factor "12" has been determined empirically (see inset of Fig. 7A). This empirical value depends on the specific numerical values we choose for the parameters, but an analytic formula for the ergodic distribution of B may be obtained by solving for the stationary distribution of the corresponding Fokker–Planck equation (Gillespie, 2002; Lindner et al., 2004 - beyond the scope of this analysis). Nonetheless, if we draw N independent identically distributed samples of $B(T)$, for $T \in [T_0, T_1]$ with $\Delta T = T_1 - T_0$ sufficiently large that $B(T)$ is ergodic, the expected maxima/minima of the samples can be estimated as $B^* \pm \kappa 12\Xi_0$ (see black dashed lines in Fig. 7A), where $\kappa = \sqrt{2}\mathrm{erf}^{-1}\left(1 - N^{-1}\right)$ is adapted from the $(1 - 1/N)^{\text{th}}$ quantile function of the normal distribution. While the above analysis holds for sufficiently small values of Ξ_0, larger amplitude noise will push the system past the stable manifold of the middle saddle in such a way that the process is no longer ergodic. When this occurs, the system undergoes a large excursion in order to return to the stable smooth motile equilibrium. This leads to a behaviour which is quite similar to the oscillatory regime, but where the period with $V > 0$ is variable in duration due to the "oscillations" being initiated stochastically (see Fig. 7B).

We note here that these transient excursions from the stable fixed point are only observed for small-to-medium levels of noise, as large amplitude noise tends to dominate over the intrinsic dynamics of the model. As we move from SN2 to SN1, the distance between the stable fixed point and the stable manifold of the saddle lying between SN1 and SN2 increases, requiring increasingly higher noise intensity to induce transient excursions. Thus as $d \to d_{\text{SN1}}$, transient excursions become increasingly less likely. Therefore, the region where stochastic oscillations may be observed is considerably smaller than the region labeled as the type IV excitable regime, and is likely a narrow band below HM1 in Fig. 3.

4.4. The oscillatory regime

4.4.1. The folded singularities

As discussed previously, the full system exhibits fast and slow epochs governed by the dynamics of the fast and slow variables, respectively. For $d_{\text{SNP}} < d < d_{\text{HB2}}$, the system (6)–(8) has a limit cycle as its sole attractor. Within a very small subset of this regime of size $\mathcal{O}(\Delta d) = 10^{-5}$, the system exhibits canard orbits where it spends a significant amount of time traveling along the unstable sheet S_V^r (see Fig. 8). Such an observation is surprising given that S_V^r is a repelling sheet, and thus by definition we expect trajectories of this system to travel away from S_V^r (e.g., see Section 4.1). To further understand this phenomenon, we use here canard theory by restricting our analysis of the dynamics of system (6)–(8) to the critical manifold. This is done by considering the reduced problem, given by

$$0 = f := (1 + \eta_B V(B)) - \frac{B}{1 + AB/(1 + M + KB)} \tag{11}$$

$$\frac{d}{dT}A(T) = g_A := d - \frac{(1 + \eta_A V + \eta_M MV)A}{1 + M + KB} \tag{12}$$

$$\frac{d}{dT}M(T) = g_M := RB - (\theta + \eta_M V)M, \tag{13}$$

which can be obtained from Eqs. (6)–(8) by taking the limit as $\epsilon \to 0$. This is formally equivalent to saying that the fast variable B is projected onto the critical manifold S. As can be seen in Fig. 8, the canard orbits travel along the critical manifold, passing over the fold which joins S_0 and S_V^r (the lower black line in Fig. 8B). Thus in order to determine how these canards are generated, we will focus our attention on the dynamics of the reduced problem as it passes over the fold-curve F^-. Generically, fold-points are the singularities of the reduced problem (Wechselberger, 2012), defined by

$$f(B, A, M) = 0, \quad \frac{\partial f}{\partial B}(B, A, M) = 0. \tag{14}$$

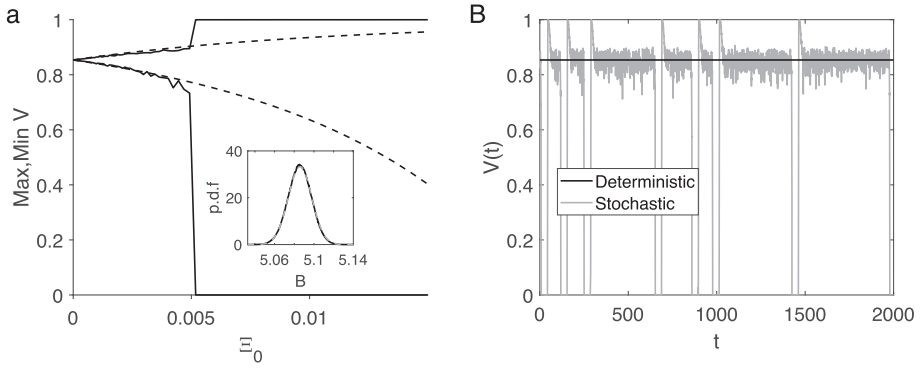

Fig. 7. Noise-dependent dynamics in the type IV excitable regime. (A) The maximum and minimum observed protrusion velocity as the noise magnitude Ξ_0 is varied (solid lines). For small values of Ξ_0, fluctuations relax back to the smooth motile equilibrium and the max/min is well predicted by evaluating $V(B^* \pm \kappa 12\Xi_0)$ (dashed lines). However for $\Xi_0 \gtrsim 0.006$, fluctuations push the system past the stable manifold of the middle saddle leading to a breakdown of the previous prediction (inset). For $\Xi_0 \lesssim 0.006$, the empirical distribution (black line) of $B(T)$ agrees very well with the theoretical probability density function of a normal distribution (grey dashed line) with a standard deviation given by $\kappa 12\Xi_0$ (here we have used $\Xi_0 = 0.007$). (B) Time series simulations of the model in the type IV excitable regime. In the absence of noise, the system remains at the motile equilibrium with protrusion velocity $V(B^*) > 0$ (black line). In the presence of noise ($\Xi_0 = 0.007$), the system is perturbed beyond the stable manifold of the saddle and it undergoes large excursions that push it below $B = B_c$, causing protrusion velocity to drop to $V = 0$ stochastically (gray line).

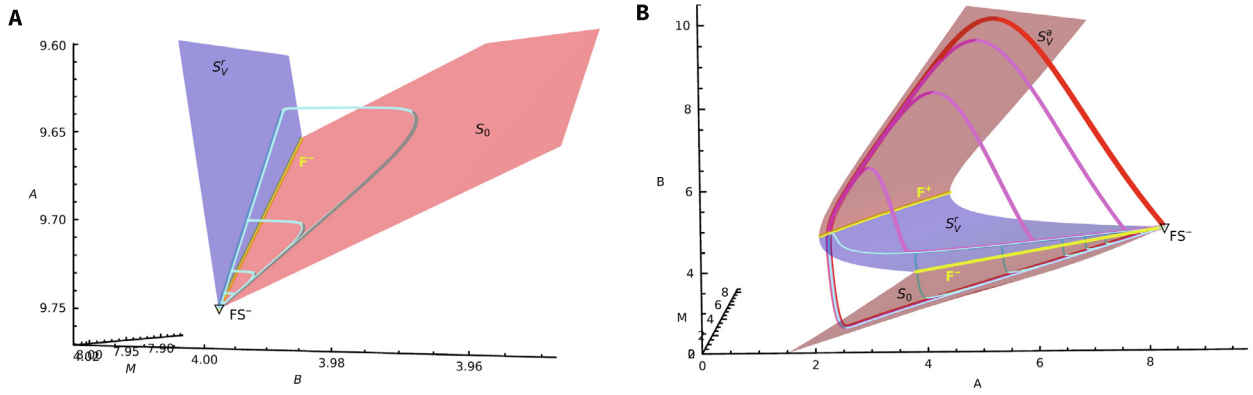

Fig. 8. The canard explosion emerging from HB1, where the stalled equilibrium changes to a saddle fixed point near the folded saddle FS^- (open triangle symbol) lying on the lower fold-curve F^- (yellow line). (A) Very close to HB1, limit cycles (cyan lines) expand with increasing d. These limit cycles are headless canard orbits as they travel first along the attracting sheet S_0 (red surface) and eventually jump up to the repelling sheet of S_V^r (blue surface) and back to the folded saddle FS^-. (B) As d continues to increase, the headless canards travel further along S_0 and S_V^r, getting closer and closer to the upper fold-curve F^+ (yellow line) on the critical manifold where S_V^r meets the attracting sheet S_V^a (red surface). The headless canard which has a peak right at F^+ is termed the maximal canard, and this canard separates the family of headless canards from the family of canards with head (magenta lines). The canards with head continue to grow by traveling further along S_V^a, until they jump down to S_V^r where they travel back to FS^-. As d grows even further, the orbits eventually become relaxation oscillations (red line) that jump between the attracting sheets S_V^a and S_0 and do not travel along the repelling sheet S_V^r. (For interpretation of the references to colour in this figure legend, the reader is referred to the web version of this article.)

Generally, away from fold-points, the fast variable B may be expressed as a function of the slow variables $B = h(A, M)$ by solving $f(B, A, M) = 0$ in Eq. (11). In other words, the critical manifold S may be represented over a single coordinate chart of the slow variables. By expressing the dynamics of B on the critical manifold, we obtain

$$\frac{d}{dT}B = \left(\frac{\partial f}{\partial B}\right)^{-1}\left(\frac{\partial f}{\partial A}g_A + \frac{\partial f}{\partial M}g_M\right).$$

At a fold-point, along either fold-curve F^- or F^+, the projection of B onto S is singular, which motivates the definition of a rescaled time variable $\tilde{T}$ with $T = \tilde{T}\, D_B f$ (where $D_B f$ is the total derivative of f with respect to B). This allows us to define the desingularized reduced problem as

$$\frac{d}{d\tilde{T}}B = \frac{\partial f}{\partial A}g_A + \frac{\partial f}{\partial M}g_M \tag{15}$$

$$\frac{d}{d\tilde{T}}A = \frac{\partial f}{\partial B}g_A \tag{16}$$

$$\frac{d}{d\tilde{T}}M = \frac{\partial f}{\partial B}g_M. \tag{17}$$

Solving for M using Eq. (11), we obtain

$$M = M_{\text{crit}}(A, B) := \frac{AB(1+\eta_B V(B))}{B-(1+\eta_B V(B))} - BK - 1.$$

This expression can be used to reduce the 3-dimensional system, given by Eqs. (15)–(17), into 2-dimensional system by eliminating, without loss of generality, this slow variable. Substituting the expression for M into Eq. (9), we obtain the desingularized system (i.e., the desingularized reduced problem projected onto the critical manifold), given by

$$\frac{d}{d\tilde{T}}B = -\frac{B+\sigma_1}{AB^2\eta_B}[B\eta_B(B(\theta K+R)+\theta+1) \tag{18}$$
$$\sigma_1\eta_B(B(\theta(A+K)+d+R)+\theta+1) - (\sigma_1+1)\eta_A(B+\sigma_1)]$$

$$\frac{d}{d\tilde{T}}A = \frac{\sigma_2}{AB^3\sigma_1\eta_B}[(\sigma_1+1)\eta_M(B(\sigma_1(A+K)+BK+1)+\sigma_1) \tag{19}$$
$$+\eta_B(Bd\sigma_1+B+\sigma_1)+(\sigma_1+1)(-\eta_A)(B+\sigma_1)],$$

where $\sigma_1 = -(1+\eta_B V(B))$ and $\sigma 2 = AB^2\eta_B V'(B) - \sigma_1^2(A+K) - B^2K - 2BK\sigma_1$. By inspection of Eq. (16), we see that the desingularized system has at least two A-nullclines, one corresponding to the fold ($\partial f/\partial B = 0$) and the other corresponding to the A-nullclines of the full system ($g_A = 0$). Because we are interested in the dynamics precisely as trajectories cross the fold, we will focus on the former case, i.e., the folded singularities of the desingularized system, defined by

$$\frac{\partial f}{\partial B} = 0 \quad \text{and} \quad \frac{\partial f}{\partial A}g_A + \frac{\partial f}{\partial M}g_M = 0. \tag{20}$$

In order to find these folded singularities numerically, we isolate A in both the first and second expressions of Eq. (20) restricted to $M = M_{\text{crit}}(A, B)$, yielding

$$A = A_{\text{fold}}(B) := \frac{K(-\eta_B V(B)+B-1)^2}{B^2\eta_B V\prime(B) - \eta_B^2 V(B)^2 - 2\eta_B V(B) - 1}$$

and

$$A = \frac{1}{B\theta(\eta_B V(B)+1)}[B(\theta(-BK+K-1)-BR+d+R-1)+\theta+1$$
$$V(B)(\eta_B(B(d+\theta K+R)+\theta+1)+\eta_A\eta_B V(B) - B\eta_A+\eta_A)],$$

respectively. Using the parameters listed in Table 1 with $d = 0.750004 = d_{\text{HB1}}$, we find that these two curves intersect at

$$B^- \approx 4.00002 \quad \text{and} \quad B^+ \approx 5.19902$$

which correspond to the B-values of the two folded singularities located on F^- and F^+, respectively. We further note that although F^+ and F^- appear to be disjoint curves in Fig. 8, they actually meet at a cusp-like structure near $(B, A, M) = (4, 0, -5)$. Folded singularities can be characterized by their two non-zero eigenvalues (Wechselberger, 2012); these have determined from the Jacobian matrix of the desingularized system (18)-(19), evaluated at the two folded singularities, to be

$$FS^- = (B^-, A_{\text{fold}}(B^-), M_{\text{crit}}(A_{\text{fold}}(B^-), B^-))$$

and

$$FS^+ = \left(B^+, A_{\text{fold}}\left(B^+\right), M_{\text{crit}}\left(A_{\text{fold}}\left(B^+\right), B^+\right)\right).$$

Numerical evaluation of the Jacobian matrix reveals that both folded singularities are in fact folded saddles (see Table 2), but only the lower folded saddle FS^- is relevant to the canard orbits. The singular canard associated with FS^- (going from the attracting sheet S_0 to the repelling sheet S_V^r and passing through FS^-) determines the flow of solution close to this folded saddle.

Table 2
Folded singularities of the desingularized system and their stability properties.

FS	(B, A, M)	$J(B, A)$	λ_1	λ_2
FS^-	(4.00002, 15.7493, 15.999)	$\begin{bmatrix} 4.88859 \times 10^{-9} & 0.0397441 \\ 0.000148825 & -0.000559416 \end{bmatrix}$	-0.0027278	0.00216839
FS^+	(5.19902, 6.96656, 14.2681)	$\begin{bmatrix} -0.00984134 & 0.0899238 \\ 0.000603317 & -0.00115534 \end{bmatrix}$	-0.00919448	0.00559321

4.4.2. Canard explosion

As can be seen in Fig. 2, the periodic envelope of this limit cycle grows very rapidly from $B \approx B_c = 4$ to $B \approx 10$ on an interval with $\mathcal{O}(\Delta d) = 10^{-5}$. This rapid growth of a limit cycle is typically referred to as a canard explosion (Desroches et al., 2012). In order to understand this phenomenon, we use here the decomposition of the critical manifold S into attracting and repelling sheets; such a decomposition is known to organize the dynamics of limit cycles during the canard explosion (Desroches et al., 2012). In a system with one fast and two slow variables, attracting and repelling sheets meet at folds of the critical manifold (see yellow lines in Fig. 8) and organize the dynamics of the limit cycles during the canard explosion (Desroches et al., 2012). From Fig. 4, we can see that there are two folds in the critical manifold. Furthermore, from what we discussed above with respect to excitability of the stalled equilibrium and the bistable regime, it is clear that, S_V^r, the lower sheet of S_V is repelling whereas, S_V^a, the upper sheet of S_V and the whole of S_0 are attracting (see Fig. 8).

Once the full system goes through a Hopf bifurcation at d_{HB1} shown in Fig. 2, the stalled equilibrium becomes a saddle fixed point (see Fig. 4C). Right at this point, periodic solution in the form of canard orbits emerge; these canard orbits are limit cycles that follow the bottom attracting sheet S_0 as well as the repelling sheet S_V^r for a significant amount of time by passing very closely to the folded saddle FS^- (open triangles in Fig. 8) determined by the desingularized reduced problem (Wechselberger et al., 2013). Initially, the limit cycles travel away from FS^- along S_V^r for some time until they jump to S_0 where they travel back towards FS^- to complete the orbit (see Fig. 8A). As d increases, the orbits grow in size and approach the fold that separates S_V^r and S_V^a. Near this fold, the limit cycles begin to jump upwards to S_V^a. They then move along S_V^a down towards the fold. Once they reach the fold, they jump down to S_0 where they move back towards the folded saddle (see Fig. 8A). As d continues to increase, the point at which orbits jump up to S_V^a moves closer to FS^- such that for $d \gtrsim d_0 + 10^{-5}$, the limit cycle spends negligible time traveling along the repelling sheet of the manifold (i.e., the limit cycles are no longer canard orbits, see red line in Fig. 8).

5. PDE model simulations

We now turn our attention to the PDE model, given by Eqs. (1)–(3), in order to see how the analysis of the simplified ODE model carried out in the previous sections can be used to understand the underlying dynamics of the PDE model. We recall that the simplified model is obtained by making two simplifications to the PDE model: (i) the diffusion-like term that accounted for the lateral movement of actin filament tips due to polymerization is dropped; and (ii) the formalism used to determine the critical barbed actin density B_c, as described by Eq. (5), is simplified by setting $B_c = B_c^0$. The first modification transforms the model into a system of first order ODEs whose oscillatory regime corresponds to traveling waves of protrusion for the PDE model. The second modification, on the other hand, is somewhat more subtle and requires further investigation.

5.1. Two-parameter diagram for the PDE model

Applying the second modification through the use of Eq. (9) is necessary to resolve some ambiguities with model definition. In particular, when using Eq. (5), it is unclear what the protrusion velocity should be for $B \in \left[B_c^0, (1+E)B_c^0\right]$. In our implementation of the PDE model, we have found that this issue may lead to rapid oscillations (period $= \mathcal{O}(\Delta t)$) in the protrusion velocity when the time step Δt becomes very small. This problem is overcome by choosing the time step such that it satisfies the constraint

$$\Delta t \partial B/\partial T|_{B=B_c^0} > EB_c^0,$$

which prevents rapid oscillations in the protrusion velocity. This choice is made due to a lack of rapid oscillations in protrusion velocity in the numerical results of Barnhart et al. (2017). However, such a choice in time step is somewhat inconsistent, and not very practical for the numerical continuation methods used in the bifurcation analysis. Therefore, to circumvent this issue we have opted to analyze the ODE model with a single value of B_c (hence the use of Eq. (9)).

From Eq. (5), it is clear that B_c can attain two distinct values B_c^0 and $(1+E)B_c^0$, whenever $B < B_c^0$ and $B > B_c^0$, respectively. However, it is somewhat less clear which value of B_c is relevant for delineating the boundaries of model behaviour for the PDE model. In order to clarify this, we have computed two-parameter bifurcation diagrams for the ODE model, setting $B_c = B_c^0$ or $B_c = (1+E)B_c^0$, and then compared the resulting bifurcation diagrams to the regimes

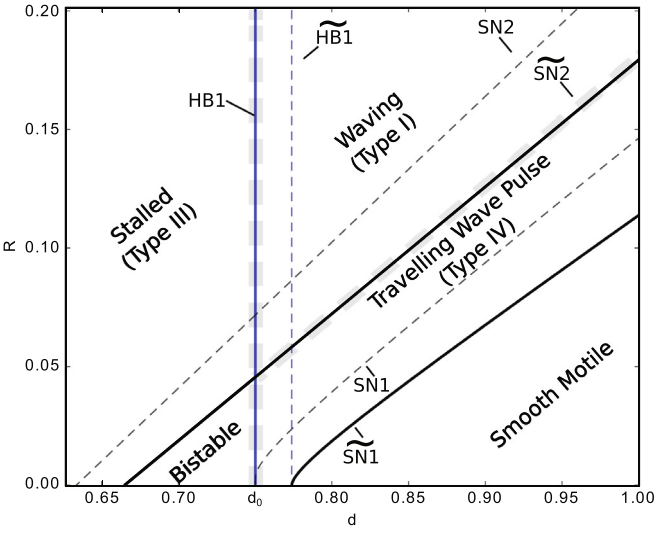

Fig. 9. Two-parameter bifurcations of the ODE model identify the various regimes of behaviour of the PDE model. Briefly, two-parameter bifurcations similar to that in Fig. (3) are computed with $B_c = B_c^0$ and $B_c = (1+E)B_c^0$. Bifurcations associated with the latter value of B_c are denoted with tildes (e.g., SN2). Bifurcations which coincide with those identified with the PDE model are depicted by solid lines while those that do not coincide are depicted by thin dashed lines. The boundaries of the various regimes of behaviour associated with the PDE model identified in Barnhart et al. (2017) are overlaid as thick grey dashed lines.

of behaviour obtained by the PDE model in Barnhart et al. (2017). In Fig. 9, we show the boundaries of the two-parameter bifurcations that match those identified by the PDE model as solid lines whereas the ones that do not match as thin dashed lines. The most relevant boundaries have been determined by two methods: (i) by extensive testing of the PDE model behaviour on both sides of each boundary determined by the two-parameter bifurcation, and (ii) by comparison to the two-parameter regimes identified in Barnhart et al. (2017) (see thick dashed lines in Fig. 9). As can be seen, the PDE model changes its behaviour at boundaries defined by both values of B_c; namely, B_c^0 (whose bifurcations are denoted without tilde, e.g., HB1) and $(1+E)B_c^0$ (whose bifurcations are denoted with tildes, e.g., $\widetilde{\text{SN}}2$). In other words, the underlying dynamics of the PDE model is a hybrid of the two corresponding simplified ODE models. As we have seen in Section 3.1, the stalled equilibrium crosses $B = B_c^0$ at d_0. Therefore, for $d \leqslant d_0$, regimes of behaviour associated with $B_c = B_c^0$ are relevant in determining outcomes of the PDE model, while for $d > d_0$, we find that the boundaries associated with $B_c = (1+E)B_c^0$ are relevant in delineating the regimes of behaviour (see Fig. 9). The exception to this rule is the bistable regime, whose left boundary is defined by $\widetilde{\text{SN}}2$ despite having $d < d_0$.

Based on this, we can conclude that the PDE model defines five parameter regimes identical to those obtained using the ODE model; that includes (i) a stalled regime that corresponds to the stalled, type III excitable regime in the ODE model; (ii) a waving regime that corresponds to the oscillatory, type I excitable regime in the ODE model; (iii) a bistable regime as in the ODE model; (iv) a smooth motile regime as in the ODE model; and (v) a traveling wave pulse regime that corresponds to the type IV excitable regime in the ODE model. Here we distinguish between the oscillatory dynamics of the ODE model (i.e., the purely temporal phenomenon) and the waving dynamics of the PDE model (i.e., the spatiotemporal phenomenon that exhibits traveling waves). This distinction motivates the label of traveling wave pulse regime in the PDE model for type IV excitability. It is important to note here that, based on the properties discussed in Sections 4.1 and 4.3, the stalled, bistable, and traveling wave pulse regimes are all capable of producing spatiotemporal patterns in the presence of noise. This will be investigated in more detail in the following sections.

5.2. The effects of noise in the traveling wave pulse regime

As we have repeatedly stated in Sections 3 and 4 with the folded nature of the bifurcation structure, there exists a parameter regime (labeled type IV excitable regime) where the ODE is very sensitive to noise. In this regime, deterministic realizations of the model will all converge to the smooth motile equilibrium, while stochastic realizations will exhibit large excursions that lead to a temporary halt in protrusion when the magnitude of noise is sufficiently large (see Fig. 7). In order to understand how such dynamics manifest themselves with the PDE model, we investigate here how it behaves in this parameter regime. While it was previously demonstrated that the PDE model, in its waving regime, is capable of propagating a wave of protrusion (Barnhart et al., 2017), its behaviour in the traveling pulse regime remains incompletely explored. In particular, we wish to know what will occur when a single spatial point is stochastically pushed below the stable manifold of the saddle, transiently blocking that single point from protruding. Will the "unexcitedness" of that point spread outwards, leading to widespread halt in protrusion? Or will the excited state of the neighbouring points simply fill the zone of depleted B, such that the leading edge will only pause briefly at random points from time to time?.

In order to answer these questions, we have implemented the PDE model on a domain of length $L = 40$ with a spatial step $\Delta X = 0.1$ and a time step $\Delta T = 0.01$. Time integration of the model was carried out using a second order Adams–Bashforth integrator (Griffiths and Higham, 2010) that can successfully deal with nonlinear reaction terms in a computationally efficient manner. The diffusion-like transport term in Eq. (1) and the boundary conditions on B are implemented by an appropriate combination of forward and backward differences for the inner and outer differential operators, respectively.

In the absence of noise, simulations of the PDE model in the traveling wave pulse regime exhibit a smooth motile behaviour with the whole domain protruding indefinitely (results not shown). However, as discussed in Section 4.3, once noise is turned on ($\Xi_0 \geqslant 0.0006$), random fluctuations push the system below the stable manifold of the middle saddle (i.e., the right saddle in Fig. 6) at discrete points in the domain. This leads to a temporary stalling of protrusion which spreads laterally just like protrusion does during the initiation of a wave of protrusion (see Fig. 10). This indicates that the transport term $\partial_x\left(\Gamma^{-1}\partial_X B\right)$ in the PDE model can propagate both protrusion initiation and termination events.

5.3. Rough motility

The irregular nature of the protrusions observed in the traveling wave pulse regime raises the question of whether or not it is related to the "rough" mode of motility described in Barnhart et al. (2017). In this experimentally observed waving mode of motility, a wave of protrusion starts from a single point and spreads outwards to produce diagonal stripes of finite width in kymographs similar to that shown in Fig. 10A. However, rough motility is characterized by the stochastic termination of traveling waves of protrusion (i.e., breaks in the diagonal stripes). This termination of traveling waves has been studied extensively in the field of excitable media (e.g., the actin cytoskeleton) (Keener and Sneyd, 2009). Due to the intrinsic properties of excitable systems, when waves of protrusion collide with one another, either one (or two) wave(s) will emerge from the collision or they will both annihilate (Beta et al., 2020). Alternatively, a protrusion wave may also terminate due to collision with a refractory region, a state in which the system requires higher amplitude stimulation to exhibit excitability.

In order to quantify the occurrence of each of these events, we have utilized a kymograph analysis pipeline to obtain distinct kymograph tracks (i.e., traveling waves of protrusion within kymographs similar to that shown in Fig. 11A), classified according to how they terminate. Three classifications for track terminations have been considered: (i) annihilation, (ii) collision, or (iii) refractory (see Appendix B for more details). Applying this methodology to simulation data obtained from the traveling wave pulse regime reveals that, when noise magnitude is sufficiently high, protrusion waves primarily terminate through annihilation in the traveling wave pulse regime (see red x symbols in Fig. 11B).

At very low levels of noise, waves do not collide; instead, we see stochastically-induced termination events that propagate along the leading edge (see Fig. 11A). However, as we increase the noise magnitude, the waves of protrusion become increasingly distorted with multiple protrusion waves being initiated at the same time and occasional annihilation termination events. By increasing noise further, wave initiation becomes less synchronized across space, leading to an increase in waves colliding and annihilating with one another (see Fig. 11B). Wave termination by collision with refractory zones is also observed, but much less frequently than annihilations (see green + symbols in Fig. 11B). If we continue to increase noise, the propagation of protrusion waves becomes less obvious (see Fig. 11C), until at very high noise the whole

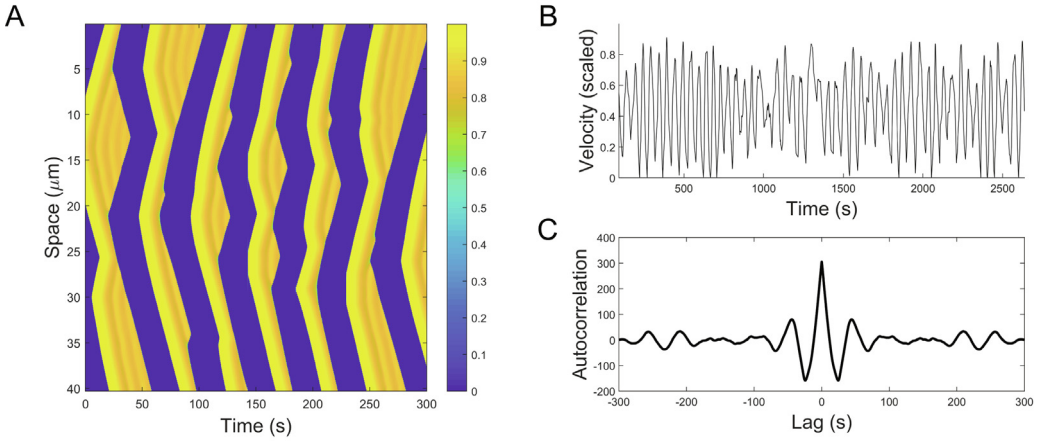

Fig. 10. The dynamics of the PDE model in the traveling wave pulse regime with additive noise. Here we have used $d = 1.95979$, $R = 0.8$, and $\eta_A = \eta_M = 0.5$ with $\Xi_0 = 0.0006$. (A) Kymograph of protrusion velocity exhibits traveling wave behaviour where the temporal duration of protrusion can be highly variable even within the same wave. (B) Mean protrusion velocity fluctuating stochastically with respect to time. (C) Mean autocorrelation function of the protrusion velocity.

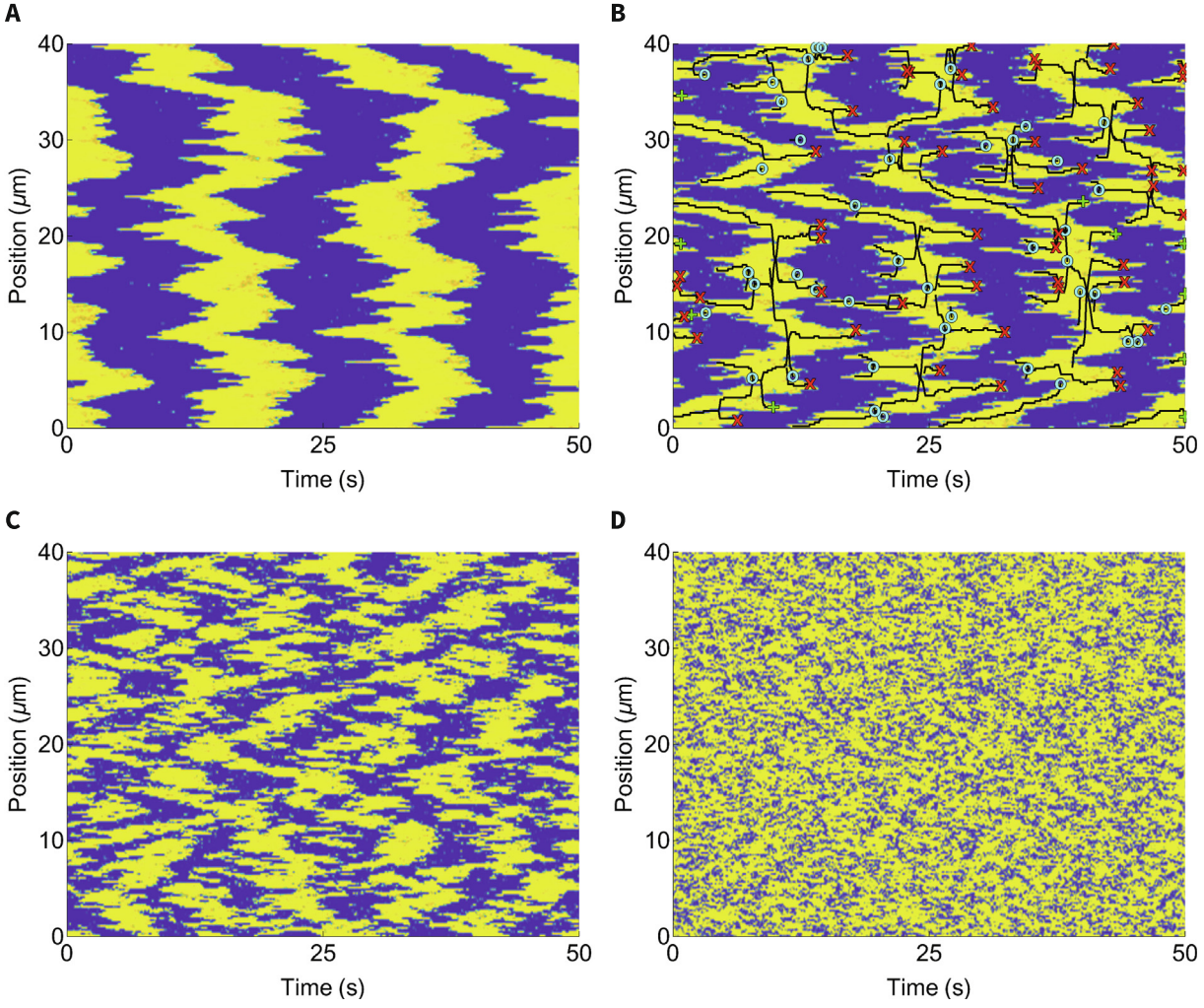

Fig. 11. The effect of noise in the traveling wave pulse regime. Kymographs of protrusion velocity with $R = 0.8, d = 1.95979$ and (A) $\Xi_0 = 1e-1$; (B) $\Xi_0 = 1.5e-1$; (C) $\Xi_0 = 3e-1$; (D) $\Xi_0 = 1$. In panel B, we have overlaid kymograph tracks generated by the pipeline as black lines. Track termination events are classified according to the criteria in Appendix B, where annihilation events are labeled with red "x" symbols, collision events with cyan "o" symbols, and refractory events with green "+" symbols.

leading edge protrudes and stalls in a completely stochastic manner (see Fig. 11D). It should be noted here that such behaviour, characterized by the absence of distinct propagating waves and the observation of the whole of the leading edge to be primarily protrusive, is common to all other regimes of system (1)–(3) when noise becomes sufficiently large.

The annihilation-dominated behaviour described above is considerably different from the spatiotemporal patterns of protrusion observed in kymographs associated with the stalled (Fig. 12C) and bistable (Fig. 12B and D) regimes. Consistent with previous findings (Barnhart et al., 2017), the termination of protrusion waves in the stalled regime is primarily caused by collisions with refractory zones (see green + symbols in Fig. 12 B). On the other hand, in the bistable regime, wave termination occurs due to a mixture of annihilation and refractory collision events (Fig. 12D). Compared to the traveling wave pulse regime, these two former regimes produce much more clearly defined traveling waves of protrusion over larger ranges of noise magnitude (see Fig. 12A-D), unlike the waves in the traveling wave pulse regime that become increasingly packed and hard to discern (see Fig. 11).

In order to compare these two different spatiotemporal patterns of protrusion produced by numerical simulation to the experimental phenomenon of rough motility, we have used the same pipeline designed to analyze kymographs to characterize the kymograph associated with rough motility (see left panel in Fig. 13A, adapted from Fig. 1F in Barnhart et al. (2017)). Our results reveal that rough motility exhibits a mixture of annihilation and refractory kymograph track termination events (see Fig. 13B), with roughly equal probability. Based on this, we conclude that the bistable regime appears to be the most compatible with the experimentally observed patterns of protrusion.

While the spatiotemporal dynamics of the PDE model suggest that the bistable regime is a likely a candidate for rough motility, we may also draw a similar conclusion based on population statistics of the modes of motility. Experimental manipulations in Barnhart et al. (2017) suggested that the parameter regime associated with rough motility should grow in size as the maturation rate of adhesions R is decreased (see right panel in Fig. 13A, adapted from Fig. 1M in Barnhart et al. (2017)). This assumption may be justified by considering the heterogeneity of a population of cells as a set of points in parameter space (e.g., see the blue and pink ellipses in Fig. 13C for an illustration in (d, R)-space). Plating cells on a substrates of varying adhesiveness corresponds conceptually to varying the R parameter-value of a population of cells, where substrates with a high (medium) adhesiveness corresponds to a larger (smaller) value of R highlighted by the blue (pink) ellipses in Fig. 13. This means that populations of cells plated on substrates of varying adhesiveness will have differing proportions of cells in the distinct parameter regimes identified above. Given this perspective, it seems most likely that rough motility is produced by the bistable regime, as it is the only regime which grows with decreasing R. We therefore conclude, based on these two

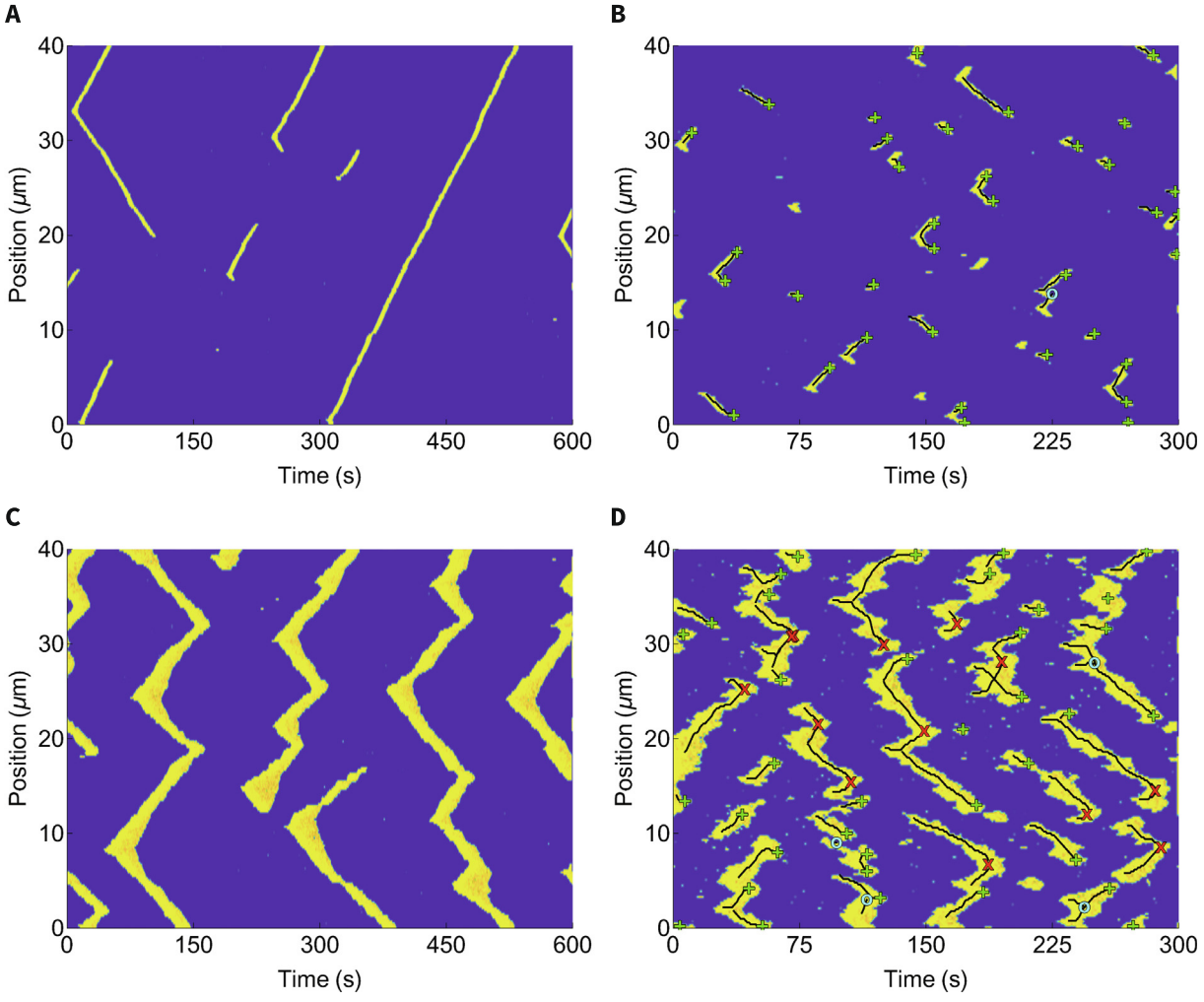

Fig. 12. The effect of noise in (A&B) the stalled regime with $R = 0.2$ and $d = 0.7$, and (C&D) bistable regime with $R = 0.02$ and $d = 0.71$. Kymographs of protrusion velocity with (A) $\Xi_0 = 4e-2$; (B) $\Xi_0 = 7e-2$; (C) $\Xi_0 = 5e-2$; (D) $\Xi_0 = 8e-2$. In panels B and D, we have labeled kymograph tracks generated by the pipeline and their termination events according to the same scheme as in Fig. 11.

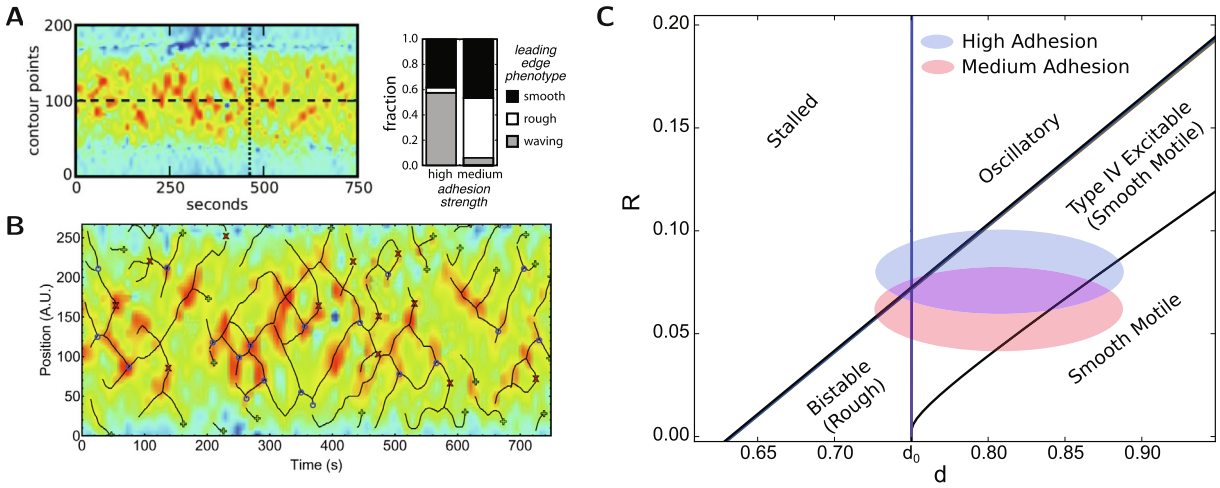

Fig. 13. Population level dynamics as predicted by the PDE model defined by Eqs. (1)–(3). (A) Experimental data adapted with permission from Barnhart et al. (2017). Left: Kymograph of protrusion velocity for a cell undergoing rough motility (Fig. 1F in Barnhart et al. (2017)). Right: bar graph depicting changes in population-level statistics of the modes of motility on substrates with medium and high levels of adhesion (Fig. 1M in Barnhart et al. (2017)). (B) Kymograph analysis of the data in panel A (left), using the pipeline (see Fig. 11 for the labeling scheme). (C) Qualitative depiction of the intercellular heterogeneity in (d, R)-parameter space. A population of cells plated on substrates of high (medium) adhesiveness is depicted as a blue (pink) ellipse. By varying the value of adhesion maturation rate R of a population of cells, produces a shift in population dynamics. The size of the sub-populations within each ellipse, defined by the five distinct parameter regimes described in Fig. 3, get altered as a result. (For interpretation of the references to colour in this figure legend, the reader is referred to the web version of this article.)

arguments, that the bistable regime is the most compatible with the rough mode of motility.

6. Discussion

We have analyzed in detail the underlying dynamics of a model of traveling waves of protrusion that arise due to actin polymerization in the lamellipodium. By underlying dynamics, we specifically mean the spatiotemporal PDE model (1)–(3) without its spatial term $\partial_x\left(\Gamma^{-1}\partial_x B\right)$, which yields a simpler system of ODEs. This spatial term appears at first to be a diffusion-like term as it contains the second spatial derivative of the barbed actin tip density B. However, since $\Gamma = \Gamma(B)$, this spatial transport term is somewhat more complicated than that. In fact, it represents the advective transport of barbed actin tips due to polymerization which is not obvious from its form in Eq. (1) (Lacayo et al., 2007). Therefore, our analysis of the ODE system gives us insight into the intrinsic dynamics of the system independent of any spatial considerations, where we may assume that any significant spatial gradient in B is advected (i.e., transported with a constant speed) along the leading edge to produce traveling waves of elevated or depleted B. Anecdotally, we have observed that this gradient must be sufficiently steep to propagate with appreciable speed, and investigation of wave-speed should be pursued further to gain a more complete understanding of the model.

The primary objectives for this study were to (i) decipher the excitability properties of the ODE model (6)–(8)), (ii) determine the bifurcation points that define the boundaries of all the regimes of behaviour exhibited by the PDE model, and (iii) understand the model's connection to rough motility in more detail. Through this analysis, we successfully identified in both the ODE and PDE models the three original regimes of behaviour found in Barnhart et al. (2017), namely, stalled, waving and smooth motile regimes, and discovered two new ones, namely the bistable and traveling wave pulse regimes.

When analyzing kymographs of the experimental data in Barnhart et al. (2017), we used a pipeline capable of distinguishing between the three termination events seen in kymographs tracks: annihilation, collision, and refractory; this revealed that the dynamics of rough motility exhibits approximately equal mixture of refractory and annihilation wave terminations. The traveling wave pulse regime was initially thought to be a good candidate for explaining rough motility seen in fish keratocytes because of its sensitivity to noise. However, after further examination of this regime using the same pipeline, we found that it predominantly produces traveling waves of protrusion that are not compatible with rough motility (see Fig. 11) and it has an inappropriate shape in (d, R)-space (see Fig. 3.3). In Barnhart et al. (2017), it was hinted that the stalled regime could explain rough motility. However, our kymograph analysis suggested that its spatiotemporal dynamics exhibit primarily refractory wave termination events.

Interestingly, our kymograph analysis of the newly-identified bistable regime showed that it can produce a mixture of refractory and annihilation wave termination events, and that it has a shape in (d, R)-space that is most compatible with experimentally obtained population statistics (see Fig. 13). The latter was assessed by evaluating population shifts in parameter space while decreasing the maturating rate of NAs (assumed to be reflective of less adhesive substrates). Based on this analysis, it seems most likely that rough motility is caused by cells being in the bistable regime. We note that the ratio of annihilations to refractory terminations in the bistable regime seems to be controlled by the system's closeness to HB1, with annihilations becoming more frequent close to that bifurcation. This finding is in agreement with our characterization of the traveling wave pulse regime which is bounded to the left by HB1. Given that some periods of the experimental recording shown in Fig. 13C predominantly exhibit annihilations while others predominantly exhibit refractory collisions, it is possible that there exists some slow process that modulates closeness to HB1, leading to this apparent switching in qualitative behaviour.

We do wish to note here that noise has been treated as an extrinsic parameter than can be varied from arbitrarily small values to arbitrary large ones. However, it would be quite important to determine the noise magnitude from the intrinsic dynamics of the chemical reactions (Gillespie, 2002). Perhaps with such considerations, the traveling wave pulse regime may behave differently. However, as it stands, we cannot reconcile the traveling wave pulse regime with rough motility without applying some rather contrived assumptions on noise magnitude.

One peculiar feature of the ODE model analyzed in this study is its ability to produce canard orbits governed by a folded-saddle. These canard orbits were investigated here by analyzing both the layer problem and the desingularized reduced problem. The layer problem was formed by assuming that the slow variables are constants, while the desingularized reduced problem was obtained initially by setting the fast variables to steady state (forming the reduced problem) followed by rescaling time to remove singularities. It is important to point out here that the reduced problem define the critical manifold of the system. Applying this approach allowed us to characterize the folded singularities responsible for generating the observed canards and to identify how they are generated.

Due to the ambiguity in the definition of critical barbed end density B_c introduced in Eq. (5), we introduced a new definition of the velocity V in Eq. (9) that resolved the issue of continuity. Nonetheless, Eq. 5 shows that B_c can attain two different values: B_c^0 and $(1+E)B_c^0$. Determining which one of these is more critical in delineating the dynamics of the PDE model was one of the questions that we tackled in this study. Given that each value of B_c can produce its own set of bifurcation points in the parameter space defined by R and VASP delivery rate d, we decided to apply the continuation method using both sets of bifurcation points and compare the results to the boundaries of the regimes of behaviour obtained by the PDE model. Our results showed that, when plotting the two-parameter bifurcations of the ODE model in (d,R)-plane, some boundaries of the three original parameter regimes identified in Barnhart et al. (2017) coincided with those defined with the lower value of B_c while the others coincided with those defined by the other value. This highlights the importance of using the formalism introduced in Eq. (9) and the relevance of simplifying the PDE model into an ODE model to decipher dynamics more precisely.

The dynamics of NA maturation in the PDE model were described using a simplified ODE formalism that accounts for the birth, decay and drift of NAs but neglects the effect of mechanical force on the system, an important aspect of NA dynamics. Theoretical models of NAs have mainly focused on how mechanochemical perturbations of stable adhesions lead to different modes of growth or shrinkage (MacKay and Khadra, 2020); however, the dynamics of adhesion assembly from a single molecular complex to its macromolecular steady state remains poorly understood, particularly when the chemical bonds involved are under tension. We previously developed a biophysical model of NAs to elucidate the effect of mechanical stress on the dynamics of adhesion assembly and showed, using bifurcation theory and stochastic simulations, what the mechanical conditions are necessary for the assembly and disassembly of these NAs (MacKay and Khadra, 2019). Understanding how the dynamics of this model affect the spatiotemporal patterns of activity seen in motile cells remains to be seen. This can be accomplished through coupling such biophysical model with the ODE model presented here.

CRediT authorship contribution statement

Laurent MacKay: Conceptualization, Formal analysis, Investigation, Methodology, Software, Visualization, Writing - original draft, Writing - review & editing. **Etienne Lehman:** Conceptualization, Formal analysis, Investigation, Methodology, Visualization. **Anmar Khadra:** Conceptualization, Formal analysis, Funding acquisition, Methodology, Project administration, Resources, Supervision, Writing - original draft, Writing - review & editing.

Declaration of Competing Interest

The authors declare that they have no known competing financial interests or personal relationships that could have appeared to influence the work reported in this paper.

Appendix A. Routh-Hurwitz criterion

The characteristic polynomial for system (6)–(8) evaluated at the stalled equilibrium (i.e., Eq. (10)) may be expressed as $P(s)=s^3+a_1s^2+a_2s+a_3$, where

$$a_1=\frac{\theta\left(x\epsilon\left(K+x^2\right)+R+x\right)+\theta^2(K+x)+Rx^2\epsilon}{\theta(K+x)+R}$$
$$a_2=\frac{\theta x\left(\theta+\epsilon\left(\theta K+R+(\theta+1)x^2\right)\right)}{\theta(K+x)+R}$$
$$a_3=\frac{\theta^2x^3\epsilon}{\theta(K+x)+R},$$

with $x=1-d$. Let $z=a_1a_2-a_3$; in order to satisfy the Routh-Hurwitz stability criterion, we must show that $a_1,a_3>0$ and $z>0$. Assuming that all model parameters are positive, the first two conditions are satisfied under the constraint $x>0\iff d<1$. Therefore, we must show that $z>0$ with z is given by

$$z=\frac{\theta x}{(\theta(K+x)+R)^2}\Big[\left(\theta\left(x\epsilon\left(K+x^2\right)+R+x\right)+\theta^2(K+x)+Rx^2\epsilon\right)\left(\theta+\epsilon\left(\theta K+R+(\theta+1)x^2\right)\right)$$
$$-\theta x^2\epsilon(\theta(K+x)+R)\Big].$$

Notice that $z>0$ if the expression inside the square brackets is positive, and that this expression may be decomposed into the sum of one positive term (the first one) and one negative term (the second one). Thus we must simply show that the first term is larger than the second. Expanding in θ, the first term is given by

$$R^2x^2\epsilon^2+Rx^4\epsilon^2$$
$$+\theta\left[KRx^2\epsilon^2+x^2\epsilon\left(x\epsilon\left(K+x^2\right)+R+x\right)+R\epsilon\left(x\epsilon\left(K+x^2\right)+R+x\right)+Rx^4\epsilon^2+Rx^2\epsilon\right]$$
$$+\theta^2\left[x^2\epsilon\left(x\epsilon\left(K+x^2\right)+R+x\right)+K\epsilon\left(x\epsilon\left(K+x^2\right)+R+x\right)\right.$$
$$\left.+R\epsilon(K+x)+x\epsilon\left(K+x^2\right)+R+x+x^2\epsilon(K+x)\right]$$
$$+\theta^3\left[x^2\epsilon(K+x)+K\epsilon(K+x)+K+x\right],$$

and the second term is given by

$$-\theta^2x^2\epsilon(K+x)-\theta Rx^2\epsilon.$$

Notice that each negative terms in the second expansion has a corresponding positive term in the first expansion. Indeed, the first (second) term in the second expansion cancels with the last term in the fourth (second) line of the first expansion. This means that $z>0$, provided $x>0$, and that $d<1$ is a necessary and sufficient condition for the stalled equilibrium to be stable (based on the Routh-Hurwitz Criterion).

Appendix B. Kymograph analysis

Kymographs of protrusion velocity were obtained by numerical simulation of Eqs. (1)–(3) or through digitization of figures in Barnhart et al. (2017). In order to make these images suitable for automated analysis, we employed some pre-processing steps to clean up the images and thin out the blotches of protrusion. These pre-processing steps were carried out using MATLAB 2018a (Matlab Version, 2018); that included: (1) colormap inversion of RGB images to convert them to greyscale (rgb2ind() in MATLAB), (2) binarization of images through simple thresholding, (3) skeletonization (bwskel() in MATLAB). These skeletonized images were

then loaded into Mathematica and segmented into groups of connected kymograph tracks (MorphologicalComponents[] in Mathematica). These kymograph segments were then analyzed using KymoButler in Mathematica (Jakobs, 2019), a recently-published automated kymograph analysis software that uses deep learning.

Tracks from all segments were then classified according to specific criteria. Firstly, we defined a threshold t that allowed us to asses these criteria. If a track traveled a vertical distance less than $t/2$ since it last came within a euclidean distance t of another track, then this former track was classified as having been annihilated. This means that the remaining tracks terminated either through a collision with another track or through a collision with a refractory zone. If a non-annihilated track terminated with a euclidean distance less than t from another track, it was classified as a having collided with that other track. Otherwise, the track was classified as having terminated by collision with a refractory zone. These criteria thus defined the three track termination types described herein, namely, (i) annihilation, (ii) collision and (iii) refractory, respectively. Finally, we used $t = 12$ for the kymographs in Fig. 11, $t = 6$ for Fig. 12, and $t = 8$ for Fig. 13. The codes for this pipeline along with other simulations are available here (MacKay et al., 2020).

References

Alexander, R.P.D., Mitry, J., Sareen, V., Khadra, A., Bowie, D., 2019. Cerebellar stellate cell excitability is coordinated by shifts in the gating behavior of voltage-gated na+ and a-type k+ channels, eNeuro 6.https://doi.org/10.1523/ENEURO.0126-19.2019. URL: https://www.eneuro.org/content/6/3/ENEURO.0126-19.2019..

Ananthakrishnan, R., Ehrlicher, A., 2007. The forces behind cell movement. Int. J. Biol. Sci. 3, 303–317. URL: http://www.ncbi.nlm.nih.gov/pubmed/17589565 http://www.pubmedcentral.nih.gov/articlerender.fcgi?artid=PMC1893118.

Ballestrem, C., Hinz, B., Imhof, B.A., Wehrle-Haller, B., 2001. Marching at the front and dragging behind: differential alphavbeta3-integrin turnover regulates focal adhesion behavior. J. Cell Biol. 155, 1319–1332. https://doi.org/10.1083/jcb.200107107. URL: http://www.ncbi.nlm.nih.gov/pubmed/11756480 http://www.pubmedcentral.nih.gov/articlerender.fcgi?artid=PMC2199321.

Barnhart, E.L., Lee, K.-C., Keren, K., Mogilner, A., Theriot, J.A., 2011. An adhesion-dependent switch between mechanisms that determine motile cell shape. PLoS Biol. 9,. https://doi.org/10.1371/journal.pbio.1001059 e1001059.

Barnhart, E.L., Allard, J., Lou, S.S., Theriot, J.A., Mogilner, A., 2017. Adhesion-dependent wave generation in crawling cells. Curr. Biol. 27, 27–38. https://doi.org/10.1016/j.cub.2016.11.011. URL: http://www.ncbi.nlm.nih.gov/pubmed/27939309 http://www.pubmedcentral.nih.gov/articlerender.fcgi?artid=PMC5225140.

Bear, J.E., Gertler, F.B., 2009. Ena/vasp: towards resolving a pointed controversy at the barbed end. J. Cell Sci. 122, 1947–1953. https://doi.org/10.1242/jcs.038125. URL: http://www.ncbi.nlm.nih.gov/pubmed/19494122 http://www.pubmedcentral.nih.gov/articlerender.fcgi?artid=PMC2723151.

Beta, C., Gov, N.S., Yochelis, A., 2020. Why a large-scale mode can be essential for understanding intracellular actin waves. Cells 9 (6), 1533. https://doi.org/10.3390/cells9061533.

Choi, C.K., Vicente-Manzanares, M., Zareno, J., Whitmore, L.A., Mogilner, A., Horwitz, A.R., 2008. Actin and alpha-actinin orchestrate the assembly and maturation of nascent adhesions in a myosin ii motor-independent manner. Nat. Cell Biol. 10, 1039–1050. https://doi.org/10.1038/ncb1763. URL: http://www.ncbi.nlm.nih.gov/pubmed/19160484 http://www.pubmedcentral.nih.gov/articlerender.fcgi?artid=PMC2827253.

Clark, A.G., Vignjevic, D.M., 2015. Modes of cancer cell invasion and the role of the microenvironment. Curr. Opin. Cell Biol. 36, 13–22. https://doi.org/10.1016/j.ceb.2015.06.004. URL: http://linkinghub.elsevier.com/retrieve/pii/S0955067415000708.

Desroches, M., Guckenheimer, J., Krauskopf, B., Kuehn, C., Osinga, H.M., Wechselberger, M., 2012. Mixed-mode oscillations with multiple time scales. SIAM Rev. 54, 211–288. https://doi.org/10.1137/100791233.

Doedel, E.J., Paffenroth, R.C., Champneys, A.R., Fairgrieve, T.F., Kuznetsov, Y.A., Sandstede, B., Wang, X., 2007. Auto-07p: continuation and bifurcation software for ordinary differential equations. URL: http://indy.cs.concordia.ca/auto/auto97.pdf..

Doyle, A., Marganski, W., Lee, J., Goeckeler, Z., Côté, G., Wysolmerski, R., 2004. Calcium transients induce spatially coordinated increases in traction force during the movement of fish keratocytes. J. Cell Sci. 117, 2203–2214. https://doi.org/10.1242/jcs.01087. URL: http://www.ncbi.nlm.nih.gov/pubmed/10639334 http://www.ncbi.nlm.nih.gov/pubmed/15126622.

Edelstein-Keshet, L., 2016. Flipping the rac-rho switch in cell motility. Cell Syst. 2 (1), 10–12. https://doi.org/10.1016/j.cels.2016.01.005. URL: https://www.sciencedirect.com/science/article/pii/S2405471216000065.

Farjami, S., Alexander, R.P.D., Bowie, D., Khadra, A., 2020. Switching in cerebellar stellate cell excitability in response to a pair of inhibitory/excitatory presynaptic inputs: a dynamical system perspective. Neural Comput. 32, 626–658. https://doi.org/10.1162/neco_a_01261.

Gerhardt, M., Schuster, H., Tyson, J., 1990. A cellular automaton model of excitable media including curvature and dispersion. Science 247 (4950), 1563–1566. https://doi.org/10.1126/science.2321017.

Gillespie, D.T., 2002. The chemical langevin and fokker-planck equations for the reversible isomerization reaction. J. Phys. Chem. A 106, 5063–5071. https://doi.org/10.1021/jp0128832.

Griffiths, D.F., Higham, D.J., 2010. Numerical Methods for Ordinary Differential Equations. Springer London.https://doi.org/10.1007/978-0-85729-148-6..

Hanna, S., El-Sibai, M., 2013. Signaling networks of rho gtpases in cell motility. Cell. Signal. 25, 1955–1961. https://doi.org/10.1016/j.cellsig.2013.04.009. URL: http://www.ncbi.nlm.nih.gov/pubmed/23669310 https://linkinghub.elsevier.com/retrieve/pii/S0898656813001241.

Hasan, C.R., Krauskopf, B., Osinga, H.M., 2018. Saddle slow manifolds and canard orbits in r4 and application to the full hodgkin-huxley model. J. Math. Neurosci. 8, 5. https://doi.org/10.1186/s13408-018-0060-1.

Hodgkin, A.L., Huxley, A.F., 1952. Currents carried by sodium and potassium ions through the membrane of the giant axon of loligo. J. Physiol. 116 (4), 449–472. https://doi.org/10.1113/jphysiol.1952.sp004717.

Holmes, W.R., Carlsson, A.E., Edelstein-Keshet, L., 2012. Regimes of wave type patterning driven by refractory actin feedback: transition from static polarization to dynamic wave behaviour. Phys. Biol. 9, 46005. https://doi.org/10.1088/1478-3975/9/4/046005.

Huveneers, S., Danen, E.H.J., 2009. Adhesion signaling – crosstalk between integrins, src and rho. J. Cell Sci. 122, 1059–1069. https://doi.org/10.1242/jcs.039446. URL: http://www.ncbi.nlm.nih.gov/pubmed/19339545.

Jakobs, M.A., Dimitracopoulos, A., Franze, K. Kymobutler, a deep learning software for automated kymograph analysis. eLife 8.https://doi.org/10.7554/eLife.42288..

Jilkine, A., Marée, A.F.M., Edelstein-Keshet, L., 2007. Mathematical model for spatial segregation of the rho-family gtpases based on inhibitory crosstalk. Bull. Math. Biol. 69 (6), 1943–1978. https://doi.org/10.1007/s11538-007-9200-6. URL: http://www.ncbi.nlm.nih.gov/pubmed/17457653.

Keener, J., Sneyd, J., 2009. Wave propagation in excitable systems.https://doi.org/10.1007/978-0-387-75847-3_6..

Keener, J., Sneyd, J., 2009. Mathematical Physiology. vol. I, second ed., Springer..

Keren, K., Pincus, Z., Allen, G.M., Barnhart, E.L., Marriott, G., Mogilner, A., Theriot, J.A., 2008. Mechanism of shape determination in motile cells. Nature 453, 475–480. https://doi.org/10.1038/nature06952. URL: http://www.ncbi.nlm.nih.gov/pubmed/18497816 http://www.pubmedcentral.nih.gov/articlerender.fcgi?artid=PMC2877812.

K. M, B. JE, L. JJ, G. FB, The ena/vasp enigma, J. Cell Sci. 115.https://doi.org/10.1242/JCS.00218. URL: https://pubmed.ncbi.nlm.nih.gov/12432060/..

Kuo, J.-C., Han, X., Hsiao, C.-T., J.R.Y. III, Waterman, C.M., 2011. Analysis of the myosin-ii-responsive focal adhesion proteome reveals a role for β-pix in negative regulation of focal adhesion maturation. Nat. Cell Biol. 13, 383–393. https://doi.org/10.1038/ncb2216. URL: http://www.nature.com/articles/ncb2216..

L. CI, P. Z, V. MM, W. CA, F. DA, G. FB, M. A, T. JA, Emergence of large-scale cell morphology and movement from local actin filament growth dynamics, PLoS Biol. 5.https://doi.org/10.1371/JOURNAL.PBIO.0050233. URL: https://pubmed.ncbi.nlm.nih.gov/17760506/..

Lammermann, T., Sixt, M., 2009. Mechanical modes of 'amoeboid' cell migration. Curr. Opin. Cell Biol. 21 (5), 636–644. https://doi.org/10.1016/j.ceb.2009.05.003.

Lee, J., Ishihara, A., Theriot, J.A., Jacobson, K., 1993. Principles of locomotion for simple-shaped cells. Nature 362, 167–171. https://doi.org/10.1038/362167a0. URL: http://www.ncbi.nlm.nih.gov/pubmed/8450887.

Li, L., He, Y., Zhao, M., Jiang, J., 2013. Collective cell migration: implications for wound healing and cancer invasion. Burns Trauma 1 (1), 21–26. https://doi.org/10.4103/2321-3868.113331. URL: http://www.ncbi.nlm.nih.gov/pubmed/27574618 http://www.pubmedcentral.nih.gov/articlerender.fcgi?artid=PMC4994501.

Lindner, B., García-Ojalvo, J., Neiman, A., Schimansky-Geier, L., 2004. Effects of noise in excitable systems.https://doi.org/10.1016/j.physrep.2003.10.015. URL: https://www.sciencedirect.com/science/article/pii/S0370157303004228..

Lin, B., Holmes, W.R., Wang, C.J., Ueno, T., Harwell, A., Edelstein-Keshet, L., Inoue, T., Levchenko, A., 2012. Synthetic spatially graded rac activation drives cell polarization and movement. Proc. Natl. Acad. Sci. U.S.A. 109, E3668–E3677. https://doi.org/10.1073/pnas.1210295109. URL: http://www.ncbi.nlm.nih.gov/pubmed/23185021 http://www.pubmedcentral.nih.gov/articlerender.fcgi?artid=PMC3535611.

Luster, A.D., Alon, R., von Andrian, U.H., 2005. Immune cell migration in inflammation: present and future therapeutic targets. Nat. Immunol. 6, 1182–1190. https://doi.org/10.1038/ni1275.

Lyda, J.K., Tan, J.Z., Rajah, A., Momi, A., MacKay, L., Brown, C.M., Khadra, A., 2019. Rac activation is key to cell motility and directionality: An experimental and modelling investigation. Comput. Struct. Biotechnol. J. 17, 1436–1452.

MacKay, L., Khadra, A., 2019. Dynamics of mechanosensitive nascent adhesion formation. Biophys. J. 117 (6), 1057–1073. https://doi.org/10.1016/j.bpj.2019.08.004.

MacKay, L., Khadra, A., 2020. The bioenergetics of integrin-based adhesion, from single molecule dynamics to stability of macromolecular complexes. Comput. Struct. Biotechnol. J. 18, 393–416. https://doi.org/10.1016/J.CSBJ.2020.02.003. URL: https://www.sciencedirect.com/science/article/pii/S2001037019304970#b1010.

MacKay, L., Lehman, E., Khadra, A., 2020. Codes for deciphering the dynamics of lamellipodium in a fish keratocytes model. Anmar Khadra Repository. Deposited Oct 28, 2020. URL: http://www.medicine.mcgill.ca/physio/khadralab/Codes/code_JTB1.html..

Matlab version 9.4.0.813654 (r2018a) (2018)..

Mitry, J., Alexander, R.P.D., Farjami, S., Bowie, D., Khadra, A., 2020. Modeling excitability in cerebellar stellate cells: temporal changes in threshold, latency and frequency of firing. Commun. Nonlinear Sci. Numer. Simul. 82,. https://doi.org/10.1016/J.CNSNS.2019.105014. URL: https://www.sciencedirect.com/science/article/pii/S1007570419303338 105014.

Mogilner, A., Oster, G., 1996. Cell motility driven by actin polymerization. Biophys. J. 71, 3030–3045. https://doi.org/10.1016/S0006-3495(96)79496-1. URL: http://www.ncbi.nlm.nih.gov/pubmed/8968574 http://www.pubmedcentral.nih.gov/articlerender.fcgi?artid=PMC1233792.

Mori, Y., Jilkine, A., Edelstein-Keshet, L., 2008. Wave-pinning and cell polarity from a bistable reaction-diffusion system. Biophys. J. 94, 3684–3697. https://doi.org/10.1529/biophysj.107.120824. URL: http://www.ncbi.nlm.nih.gov/pubmed/18212014 http://www.pubmedcentral.nih.gov/articlerender.fcgi?artid=PMC2292363 http://linkinghub.elsevier.com/retrieve/pii/S0006349508704442.

Paszek, M.J., Boettiger, D., Weaver, V.M., Hammer, D.A., 2009. Integrin clustering is driven by mechanical resistance from the glycocalyx and the substrate. PLoS Comput. Biol. 5,. https://doi.org/10.1371/journal.pcbi.1000604 e1000604.

Pollard, T.D., Borisy, G.G., 2003. Cellular motility driven by assembly and disassembly of actin filaments. Cell 112, 453–465. https://doi.org/10.1016/S0092-8674(03)00120-X. URL: http://linkinghub.elsevier.com/retrieve/pii/S009286740300120X.

Pontes, B., Monzo, P., Gole, L., Roux, A.L.L., Kosmalska, A.J., Tam, Z.Y., Luo, W., Kan, S., Viasnoff, V., Roca-Cusachs, P., Tucker-Kellogg, L., Gauthier, N.C., 2017. Membrane tension controls adhesion positioning at the leading edge of cells. J. Cell Biol. 216, 2959–2977. https://doi.org/10.1083/jcb.201611117. URL: http://www.ncbi.nlm.nih.gov/pubmed/28687667 http://www.pubmedcentral.nih.gov/articlerender.fcgi?artid=PMC5584154.

Seetharaman, S., Etienne-Manneville, S., 2019. Microtubules at focal adhesions – a double-edged sword. J. Cell Sci. 132.https://doi.org/10.1242/jcs.232843. URL: http://www.ncbi.nlm.nih.gov/pubmed/31597743..

Stutchbury, B., Atherton, P., Tsang, R., Wang, D.-Y., Ballestrem, C., 2017. Distinct focal adhesion protein modules control different aspects of mechanotransduction. J. Cell Sci. 130, 1612–1624. https://doi.org/10.1242/jcs.195362. URL: http://www.ncbi.nlm.nih.gov/pubmed/28302906 http://www.pubmedcentral.nih.gov/articlerender.fcgi?artid=PMC5450230.

Szmolyan, P., Wechselberger, M., 2001. Canards in r3. J. Differ. Equations 177 (2), 419–453. https://doi.org/10.1006/jdeq.2001.4001.

Tang, K., Boudreau, C.G., Brown, C.M., Khadra, A., 2018. Paxillin phosphorylation at serine 273 and its effects on rac, rho and adhesion dynamics. PLOS Comput. Biol. 14, (7). https://doi.org/10.1371/journal.pcbi.1006303 e1006303.

van der Pol, B., 1926. Lxxxviii. on relaxation-oscillations. London Edinburgh Dublin Philos. Mag. J. Sci., 978–992 https://doi.org/10.1080/14786442608564127. URL: http://www.tandfonline.com/doi/abs/10.1080/14786442608564127.

van der Pol, B., van der Mark, J., 1928. Lxxii. ithe heartbeat considered as a relaxation oscillation, and an electrical model of the heart/i. London Edinburgh Dublin Philos. Mag. J. Sci. 6, 763–775. https://doi.org/10.1080/14786441108564652.

Wechselberger, M., 2012. À propos de canards (apropos canards). Trans. Am. Math. Soc. 364, 3289–3309. https://doi.org/10.1090/s0002-9947-2012-05575-9. URL: https://www.ams.org/journal-terms-of-use.

Wechselberger, M., Mitry, J., Rinzel, J., 2013. Canard theory and excitability. In: Nonautonomous Dynamical Systems in the Life Sciences. Springer International Publishing, pp. 89–132. https://doi.org/10.1007/978-3-319-03080-7_3.

Ye, F., Kim, C., Ginsberg, M.H., 2011. Molecular mechanism of inside-out integrin regulation. J. Thrombosis Haemostasis 9(Suppl 1) 20–25.https://doi.org/10.1111/j.1538-7836.2011.04355.x. URL: http://www.ncbi.nlm.nih.gov/pubmed/21781238 http://www.pubmedcentral.nih.gov/articlerender.fcgi?artid=PMC3979599..

Zaidel-Bar, R., Itzkovitz, S., Ma'ayan, A., Iyengar, R., Geiger, B., 2007. Functional atlas of the integrin adhesome. Nat. Cell Biol. 9, 858–867. https://doi.org/10.1038/ncb0807-858. URL: http://www.pubmedcentral.nih.gov/articlerender.fcgi?artid=2735470&tool=pmcentrez&rendertype=abstract.

Zheng, J.Q., ming Poo, M., 2007. Calcium signaling in neuronal motility. Annu. Rev. Cell Dev. Biol. 23, 375–404. https://doi.org/10.1146/annurev.cellbio.23.090506.123221.